

Research on High-Bandgap Materials and Amorphous Silicon-Based Solar Cells

**Final Technical Report
15 May 1994–15 January 1998**

E.A. Schiff, Q. Gu, L. Jiang, J. Lyou,
I. Nurdjaja, and P. Rao
*Department of Physics
Syracuse University
Syracuse, New York*



National Renewable Energy Laboratory
1617 Cole Boulevard
Golden, Colorado 80401-3393
A national laboratory of
the U.S. Department of Energy
Managed by Midwest Research Institute
for the U.S. Department of Energy
under Contract No. DE-AC36-83CH10093

Research on High-Bandgap Materials and Amorphous Silicon-Based Solar Cells

**Final Technical Report
15 May 1994–15 January 1998**

E.A. Schiff, Q. Gu, L. Jiang, J. Lyou,
I. Nurdjaja, and P. Rao
*Department of Physics
Syracuse University
Syracuse, New York*

NREL technical monitor: B. von Roedern



National Renewable Energy Laboratory
1617 Cole Boulevard
Golden, Colorado 80401-3393
A national laboratory of
the U.S. Department of Energy
Managed by Midwest Research Institute
for the U.S. Department of Energy
under Contract No. DE-AC36-83CH10093

Prepared under Subcontract No. XAN-4-13318-06
November 1998

Research on High Bandgap Materials and Amorphous Silicon-Based Solar Cells

Final Technical Report for a research project with Syracuse University

Eric A. Schiff, principal investigator

Qing Gu

Lin Jiang

Jonghun Lyou

Indra Nurdjaja

Prasanna Rao

Bolko von Roedern, technical monitor

NREL Subcontract XAN-4-13318-06

Period covered: May 15, 1994 - January 15, 1998.

Report submitted: August 2, 1998.

In Final Form: November 27, 1998.

Introduction

Preface

This research project had four broad objectives involving a variety of technical approaches:

- We sought a deeper understanding of the open circuit voltage V_{OC} in amorphous silicon based solar cells, and in particular for cells employing wide bandgap modification of amorphous silicon as their absorber layer. Our technical approach emphasized the development of electroabsorption measurements as a tool for probing the built-in potential of a-Si:H based solar cells.
- We sought a better understanding of the optical properties of amorphous silicon and of microcrystalline silicon materials such as used in the p^+ layer of some advanced a-Si:H based solar cells. Electroabsorption spectroscopy appears to be useful for this purpose, and was a natural extension of the built-in potential research.
- We sought to improve our understanding of the fundamental electron and hole photocarrier transport processes in the materials used for amorphous silicon based solar cells. Our technical approach was been to develop photocarrier time-of-flight measurements in solar cells.
- We aimed to improve V_{OC} in wide bandgap cells by searching for superior materials for the p -type “window layer” of the cell, and explored thin-film boron phosphide for this purpose.

In addition to the authors of this report, we have reported work which includes the contributions of several collaborators, in particular Reinhard Schwarz, Stefan Grebner, and Fuchao Wang of the Technical University of Munich, Richard Crandall, Eugene Iwaniczko, Werner Luft, Brent Nelson, Bolko von Roedern, and Qi Wang of the National Renewable Energy Laboratory, Subhendu Guha and Jeff Yang at United Solar Systems Corp., Xunming Deng at Energy Conversion Devices, Inc., Friedhelm Finger and Peter Hapke at Forschungszentrum Juelich, Nicolas Wyrsh and Arvind Shah, Universite de Neuchatel, and Jean-Baptiste Chevrier and Bernard Equer at Ecole Polytechnique, Palaiseau.

We have also benefitted from the cooperation and interest of several other scientists and organizations. In particular we thank Christopher Wronski at Pennsylvania State University, Steve Hegedus at the Institute of Energy Conversion, University of Delaware, and Murray Bennett at Solarex Corp. Thin Films Division.

Summary

- The built-in potential is a crucial device parameter for solar cells, and one which is only roughly known and understood for a-Si:H based cells. We have developed a technique based on electroabsorption measurements for obtaining quantitative estimates of the built-in potential in a-Si:H based heterostructure solar cells incorporating microcrystalline or a-SiC:H p layers. This heterostructure problem has been a major limitation in application of the electroabsorption technique. The new technique only utilizes measurements from a particular solar cell, and is thus a significant improvement on earlier techniques requiring measurements on auxiliary films.
- Using this new electroabsorption technique, we confirmed previous estimates of $V_{bi} \approx 1.0$ V in a-Si:H solar cells with “conventional” intrinsic layers and either microcrystalline or a-SiC:H p layers. Interestingly, our measurements on high V_{oc} cells grown with “high hydrogen dilution” intrinsic

layers yield a much larger value for $V_{bi} \approx 1.3$ V. We speculate that these results are evidence for a significant interface dipole at the p/i heterostructure interface. Although we believe that interface dipoles rationalize several previously unexplained effects on a-Si:H based cells, they are not currently included in models for the operation of a-Si:H based solar cells, and our hypothesis remains controversial.

- The Staebler-Wronski effect remains a major obsession for amorphous silicon scientists, since it holds out the tantalizing possibility of materials with much better properties than the stabilized materials achieved presently. We have explored the recent claim that light-soaking of a-Si:H substantially changes the polarized electroabsorption associated with interband optical transitions (and hence *not* defect transitions). If confirmed, this proposal would be very exciting, since it offers an insight into metastability which is not directly related to point defect generation. For this experiment, we developed a technique to use solar cell structures to replace the coplanar electrode structures previously employed for this type of work. We believe the new method reduces the uncertainties regarding the magnitude and direction of the electric field. We found that polarization effects in electroabsorption are *stronger* than previously expected, but we did not reproduce the light-soaking effect.
- One avenue for improving a-Si:H based solar cells is to increase the hole mobility, presumably by sharpening the valence bandtail associated with disorder. Although substantial experience has shown that the hole mobility is remarkably constant with changes in alloying for both optimized a-SiGe and a-SiC alloys, recent evidence suggests that improvements may in fact be possible. Ganguly and collaborators at Electrotechnical Laboratory in Japan has claimed large hole drift mobilities for their materials deposited in a triode plasma reactor, and we have confirmed their measurements at Syracuse. We have also made measurements of hole mobilities in hot-wire deposited a-Si:H. Some of the hot-wire samples yielded standard hole drift mobilities up to five times higher than found in conventional plasma-deposited a-Si:H. Disturbingly, no connection between these apparent improvements in materials and improvements in solar cell efficiency has been established.
- We have significantly clarified the relationship of ambipolar diffusion length measurements to hole drift mobilities in a-Si:H. The ambipolar diffusion length L_{amb} is arguably the single most influential parameter in assessing the potential of materials for incorporation as absorbers in a-Si:H based solar cells. We show how L_{amb} can be predicted from hole drift mobilities and the recombination response time of a-Si:H materials. The results are also of interest because they confirm the Einstein relation between diffusion and drift of carriers for disordered materials such as a-Si:H. The Einstein relation is assumed to be valid in device modeling, but this validity had not been established either experimentally or theoretically prior to our work.
- We have shown that *photocapacitance* measurements can be interpreted in terms of hole drift mobilities in amorphous silicon.
- We have completed a survey of thin BP:H and BPC:H films prepared by plasma deposition using phosphine, diborane, tri-methylboron, and hydrogen as precursor gases. The objective of this research has been to find out whether such films might offer a superior window layer film for application to wide bandgap a-Si solar cells. The research has shown good optical properties in a-BP:H films; our films do not have promising electrical properties.

Publications Acknowledging This Subcontract

1. "Polarized electroabsorption spectra and light soaking of solar cells based on hydrogenated amorphous silicon," Lin Jiang, Qi Wang, E. A. Schiff, S. Guha, and J. Yang, *Appl. Phys. Lett.* **72**, 1060 (1998).
2. "Photocapacitance and Hole Drift Mobility Measurements in Hydrogenated Amorphous Silicon," I. Nurdjaja and E. A. Schiff, in *Amorphous and Microcrystalline Silicon Technology - 1997*, edited by S. Wagner, *et al* (Materials Research Society, Symposium Proceedings Vol. 467, Pittsburgh, 1997), 723.
3. "Electroabsorption Spectra of Hydrogenated Amorphous and Microcrystalline Silicon," L. Jiang, E. A. Schiff, F. Finger, P. Hapke, S. Koynov, R. Schwarz, N. Wyrsh, A. Shah, J. Yang, and S. Guha, in *Amorphous and Microcrystalline Silicon Technology - 1997*, edited by S. Wagner, *et al* (Materials Research Society, Symposium Proceedings Vol. 467, Pittsburgh, 1997), 295.
4. "Summary of 4 ½ Years of Research Experience of the US Amorphous Silicon Research Teams," B. von Roedern, E. A. Schiff, J. D. Cohen, S. Wagner, and S. S. Hegedus, in *Prog. Photovolt. Res. Appl.* **5**, pp. 345-352.
5. "Electroabsorption Measurements and Built-in Potentials in Amorphous Silicon *pin* Solar Cells", L. Jiang, Qi Wang, E. A. Schiff, S. Guha, J. Yang, and X. Deng, *Appl. Phys. Lett.* **69**, 3063 (1996).
6. "Two-layer Model for Electroabsorption and Built-in Potential Measurements on a-Si:H *pin* Solar Cells," L. Jiang and E. A. Schiff, in *Amorphous Silicon Technology—1996*, edited by M. Hack, E. A. Schiff, S. Wagner, R. Schropp, and A. Matsuda (Materials Research Society, Symposium Proceedings Vol. 420, Pittsburgh, 1996), pp. 203-208.
7. "Non-Gaussian Transport Measurements and the Einstein Relation in Amorphous Silicon," Qing Gu, E. A. Schiff, S. Grebner, F. Wang, and R. Schwarz, *Phys. Rev. Lett.* **76**, 3196 (1996).
8. "Fundamental Transport Mechanisms and High Field Mobility Measurements in Amorphous Silicon," Qing Gu, E. A. Schiff, J.-B. Chevrier, and B. Equer, *J. Non-Cryst. Solids* **198--200**, 194--197 (1996).
9. "Field Collapse Due to Band-Tail Charge in Amorphous Silicon Solar Cells," Q. Wang, R. S. Crandall, and E. A. Schiff, in *Conference Record of the 21st Photovoltaics Specialists Conference* (IEEE, 1996), pp. 1113--1116.
10. "The Correlation of Open-Circuit Voltage with Bandgap in Amorphous Silicon-Based *pin* Solar Cells," R. S. Crandall and E. A. Schiff, in *13th NREL Photovoltaics Program Review*, edited by H. S. Ullal and C. E. Witt (AIP, Conference Proceedings Vol. 353, Woodbury, 1996), pp. 101--106.
11. "Progress in Amorphous Silicon PV Technology: An Update," W. Luft, H. M. Branz, V. L. Dalal, S. S. Hegedus, and E. A. Schiff, in *13th NREL Photovoltaics Program Review*, edited by H. S. Ullal and C. E. Witt (AIP, Conference Proceedings Vol. 353, Woodbury, 1996), pp. 81--100.
12. "Diffusion-Controlled Bimolecular Recombination of Electrons and Holes in a-Si:H," E. A. Schiff, *J. Non-Cryst. Solids* **190**, pp. 1-8 (1995).

13. "High-field Electron-Drift Measurements and the Mobility Edge in Hydrogenated Amorphous Silicon," Qing Gu, E. A. Schiff, Jean-Baptiste Chevrier and Bernard Equer, *Phys. Rev. B* **52**, pp. 5695--5707 (1995).
14. "Diffusion, Drift and Recombination of Holes in a-Si:H," R. Schwarz, F. Wang, S. Grebner, Q. Gu, and E. A. Schiff, in *Amorphous Silicon Technology--1995*, edited by M. Hack, *et al* (Materials Research Society, Pittsburgh, 1995), pp. 427-436.
15. "Electron Drift Mobility in a-Si:H Prepared by Hot Wire Deposition," Qing Gu, E. A. Schiff, R. S. Crandall, E. Iwaniczko, and B. Nelson, in *Amorphous Silicon Technology--1995*, edited by M. Hack, *et al* (Materials Research Society, Pittsburgh, 1995), pp. 437-442.

Table of Contents

Preface	2
Summary.....	2
Publications Acknowledging This Subcontract.....	4
Table of Contents.....	6
Table of Figures	8
Electroabsorption measurements and built-in potentials	10
Introduction	10
Summary of Heterostructure Model for Electroabsorption.....	12
Experimental Results on Cells with Microcrystalline <i>p</i> Layers.....	14
Interface Dipole Hypothesis.....	15
Heterostructure Model for Electroabsorption: Details.....	16
Polarized Electroabsorption Spectra and Light-Soaking of Solar Cells Based on Hydrogenated Amorphous Silicon	20
Introduction	20
Polarized Electroabsorption Techniques for Solar Cells.....	20
Results	22
Electroabsorption Spectra of Amorphous and Microcrystalline Silicon.....	24
Introduction	24
Experiments	25
Samples.....	25
Electromodulation Spectroscopy	26
Results	28
Discussion.....	30
Unusually Large Hole Drift Mobilities in Hydrogenated Amorphous Silicon	32
Introduction	32
Time-of-Flight Measurements in Hot-Wire Material.....	32
Specimens and Instruments.....	32
Time-of-flight measurements	33
Time-of-Flight Measurements in Triode Materials	35
Results	36
Relationship of Ambipolar Diffusion Length Measurements and Hole Drift Mobilities in a-Si:H	38
Photocapacitance and Hole Drift Mobility Measurements in Hydrogenated Amorphous Silicon.....	41

Introduction	41
Samples and Photocapacitance measurements	41
Model for photocapacitance and dispersive transport	43
Comparison of photocapacitance and drift-mobility measurement.....	45
Appendix	46
Search for Novel p⁺ materials.....	47
References	49

Table of Figures

- Fig. 1. Modulated electroabsorption signal as a function of the bias potential across the “standard” solar cell. The voltage-axis intercept has been used to estimate the built-in potential of the solar cell. Measurements at three laser wavelengths are illustrated, and show (cf. inset) that the intercept depends slightly on the measuring wavelength. _____ 10
- Fig. 2: Wavelength dependence of the electroabsorption parameter V_0 for four different types of a-Si:H based diode structure. In the simplest model V_0 is wavelength-independent, and is identified as the built-in potential. All samples have a-Si:H n^+ layers; all save the ECD sample have conventional a-Si:H intrinsic layers absorbers; the ECD had a high hydrogen dilution absorber. The USSC and ECD diodes had microcrystalline Si p^+ layers; the IEC sample has an a-SiC p^+ layer. Note that the wavelength-dependence is weakest for the Schottky barrier diode with no p^+ layer, suggesting that the wavelength dependence is associated with the varying p^+ layers. ____ 11
- Fig. 3. dE is the amplitude of the modulated electric field across a pin solar cell with a microcrystalline p^+ layer. The lower portion indicates the conduction and valence bandedges E_c and E_v across the cell, including band bending in the p^+ and intrinsic layers, band offsets, and an interface dipole Δ . _____ 12
- Fig. 4. Plot of the normalized, second harmonic electroabsorption signal dT_{2f} for three different wavelengths as a function of reciprocal capacitance in the standard cell; the data are generated by varying the reverse bias across the cell. _____ 14
- Fig. 5. (left) Electroabsorption coefficients a_i'' and a_p'' as a function of wavelength obtained for a-Si:H and for μc -Si:H:B respectively obtained in two types of cell (with standard and strongly H-diluted intrinsic layers). (right) Plot of the voltage-axis intercepts V_0 of first-harmonic electroabsorption measurements (obtained at three wavelengths) vs. the corresponding ratios of electroabsorption parameters $(a_p''/e_p)/(a_i''/e_i)$. The same two types of cells were used; the error bars indicate the standard deviation in V_0 for differing cells on the same substrate. The built-in potential is V_0 for $(a_p''/e_p)/(a_i''/e_i) = 1$ (cf. vertical line). _____ 15
- Fig. 6: Illustration of grazing incidence angle measurements of polarized electroabsorption. (left) The incident beam (shaded arrow) is refracted and transmitted as it passes through a $p-i-n$ solar cell; F denotes the macroscopic electric field, E_p and E_s denote the optical polarization. (right) Definitions of the various angles involved in analyzing the experiment: the refraction angle r , the polarization angle f , and the angle q between the external and polarization fields. _____ 21
- Fig. 7: Measurements of the electric-potential modulation DT for the transmittance T in a United Solar specimen. DT/T is plotted as a function of polarization of the incident beam. Curves are shown for four different light-soaking states of the cell. _____ 22
- Fig. 8: Polarized electroabsorption spectra for a-Si:H. (a) Measurements for the as-deposited state of a Solarex specimen; solid lines are a running average of three wavelength samples. (b) Symbols and solid lines show spectra for the Solarex specimen after 1 hour light soaking (30mW/cm^2) with a He-Ne laser (633nm). Dotted and dashed lines are the measurements reported by Weiser, *et al* (1988). _____ 22
- Fig. 9: Anisotropic/isotropic polarization ratio for electroabsorption measured during light-soaking at 30 mW/cm^2 . Measurements are shown for two a-Si:H based $p-i-n$ solar cells from different laboratories. _____ 24
- Fig. 10: Raman spectra of four samples deposited with different silane concentration with PECVD. _____ 26
- Fig. 11: The experimental electroabsorption spectra of sample made by 3% silane concentration. Guidelines are included in the figure as a simple solution for severe interference fringes. Both spectra for electrical field parallel to and perpendicular to the light beam polarization are shown in the figure. _____ 27
- Fig. 12: The electroabsorption spectra of pure amorphous silicon and mixtures of amorphous and microcrystalline silicon. _____ 29
- Fig. 13: Polarization ratio and rising edge width W versus the EA peak blue-shift. The empty dot is taken from Penchina (1965) in order to be consistent with the present data obtain by co-planar geometry. Please refer to Jiang, et al (1998) for comparison of co-planar and sandwich electrode geometry. _____ 31

- Fig. 14. (upper) Normalized transient photocurrents $i(t)d^2/Q_0V$ for holes measured at $\lambda = 590$ nm at several temperatures and constant electric field of 69.5 kV/cm. (lower) Logarithmic plot of $Q(t)d^2/Q_0V$ for the same conditions as the transients; for times sufficiently early that carriers have not yet been swept completely across the structure, the charge transient measures the time dependence of $L(t)/E$ of the hole displacement $L(t)$ to the electric field E . The intersection of each curve with the line at 2×10^{-9} cm²/V determines the transit times used to calculate a standard drift mobility. _____ 34
- Fig. 15: Normalized transient photocurrents measured at 300 K in a triode-deposited a-Si diode (c-Si:B/a Si:H/m) prepared at Electrotechnical Laboratory (505 nm illumination through the metal layer). Results are shown for 3 reverse-bias voltages. The total photocharge Q_0 was measured by integrating the 15 V transient. The transients show the characteristic features expected for sweepout of holes. _____ 35
- Fig. 16. Semilogarithmic plot of average hole drift mobility μ as a function of reciprocal temperature $1000/T$ for indicated values of displacement/field ratio L/E . Results are shown for a hot-wire (HW) sample and a conventional plasma-deposited (PECVD) sample of a-Si:H. _____ 36
- Fig. 17: Hole drift mobility for conventional plasma-deposited a Si:H (Gu, *et al*, 1994) and for “triode” plasma deposited a Si:H from Electrotechnical Laboratory. The upper two regression lines represent the triode-material; the open symbols represent prior measurements of Ganguly, *et al* (1996). _____ 37
- Fig. 18. Summary of hole drift mobility measurements at 298 K evaluated at $L/E = 2 \times 10^{-9}$ cm²/V as a function of bandgap. Solid circles: present measurements on hot-wire material from NREL. Diamonds - a-SiGe:H alloys (Nebel, *et al*, 1989). Circles - a-SiC:H alloys (Gu, *et al*, 1995). Hexagon - “triode” a-Si:H (Ganguly, *et al*, 1996). Square - a-Si:H (Gu, *et al*, 1996). Triangle - a-Si:H (Tiedje, *et al*, 1984). _____ 38
- Fig. 19: Proposed model for the relationship of hole drift and diffusion measurements. Drift measurements are made under recombination free conditions; diffusion measurements usually yield only the diffusion length L_D , which is determined by the hole diffusion truncated at the recombination time τ_R . _____ 39
- Fig. 20. Correlation of the hole diffusion coefficient D_h with the “Einstein normalized” hole drift mobility $(kT/q)\mu_h$; both are averaged from their photogeneration up to recombination at time τ_R . Measurements for four specimens over a range of temperatures and illumination intensities are indicated. The Einstein relation $D_h = (kT/q)\mu_h$ is indicated by the solid line. _____ 40
- Fig. 21: Short-circuit capacitance measurements as a function of photocurrent (at -2 V) in a Schottky diode specimen. Illumination was at 633 nm. _____ 42
- Fig. 22: DC photocurrent density J_{ph} and linear photocapacitance $C'_p(V)$ as a function of potential across the Schottky diode specimen. _____ 43
- Fig. 23: Comparison of calculations of linear photocapacitance with measurements in an a-Si:H Schottky barrier diode. The electron and hole calculations are based on time-of-flight mobility measurements and their corresponding non-dispersive and dispersive theories. The measurements were at 650 nm; the voltage bias axis for the measurements has been shifted by 0.4 V to account for the built-in potential of the diode. _____ 45
- Fig. 24: Comparison of the optical absorption properties of a thin boron-phosphide film (unknown stoichiometry) with literature values for several thin-film silicon materials. _____ 47

Electroabsorption measurements and built-in potentials

We present a technique for using modulated electroabsorption measurements to determine the built-in potential in semiconductor heterojunction devices. The technique exploits a simple relationship between the second-harmonic electroabsorption signal and the capacitance of such devices. We apply this technique to hydrogenated amorphous silicon (a-Si:H) based solar cells incorporating microcrystalline Si p^+ layers. For one set of cells with a conventional plasma-deposited intrinsic layer we obtain a built-in potential of 0.98 ± 0.04 V; for cells with an intrinsic layer deposited using strong hydrogen-dilution we obtain 1.25 ± 0.04 V. We speculate that interface dipoles between the p^+ and intrinsic layers significantly influence the built-in potential.

Introduction

The internal electric fields of amorphous silicon (a-Si:H) based *pin* solar cells are crucial to their operation as photocarrier collectors. The *built-in electrostatic potential* V_{bi} established by these fields is thus one of a cell's important device parameters. One promising approach to illustrating and estimating V_{bi} exploits electroabsorption measurements: by measuring the transmittance or reflectance of the cell as a function of an external potential V , an inference of the built-in potential can be made (Nonomura, Okamoto, and Hamakawa, 1983; Wang, Schiff, and Hegedus, 1994; Campbell, Jowick, and Parker, 1995; Jiang and Schiff, 1996; Jiang, Wang, Schiff, Guha, Yang, and Deng, 1996).

Some corresponding measurements are presented in Fig. 1. The transmittance T of a cell is modulated by a sinusoidal potential of amplitude dV ; the transmittance modulation dT_{1f} in phase with dV is then plotted as a function of the external DC potential V . One sees that the transmittance modulation dT_{1f} is

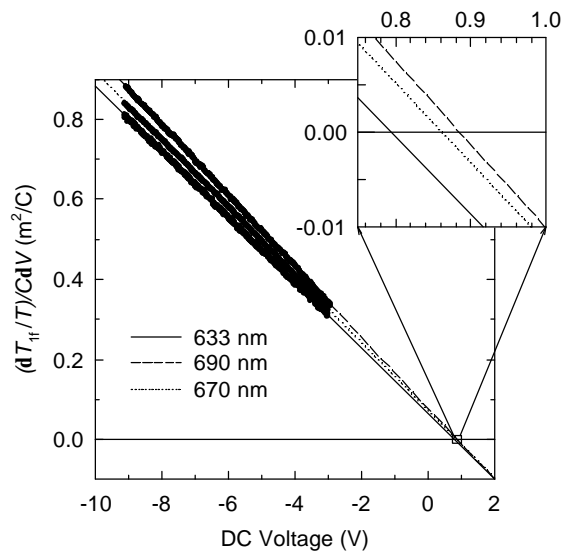


Fig. 1. Modulated electroabsorption signal as a function of the bias potential across the “standard” solar cell. The voltage-axis intercept has been used to estimate the built-in potential of the solar cell. Measurements at three laser wavelengths are illustrated, and show (cf. inset) that the intercept depends slightly on the measuring wavelength.

quite linear with the external potential. The linearity is a consequence of the fact that electroabsorption in non-crystalline materials is quadratic in electric field, and hence dT_{lf} ends up being proportional to $dV(V-V_{bi})$. The regression lines through the measurements intersect the horizontal axis near $V = 1.0$ Volts, which is an estimate of the built-in potential of this cell. The slopes of the lines indicate the strength of the electroabsorption effect at each wavelength.

As initially reported by Wang, Schiff, and Hegedus (1994), extensive signal averaging of electroabsorption measurements reveals a systematic dependence of this intercept upon wavelength; the effect is evident in the inset of Fig. 1. Wang, *et al* proposed that this wavelength-dependence is a heterostructure effect, since differing layers have differing wavelength dependences to their electroabsorption. The solar cells studied by Wang, *et al*, had a-Si:H intrinsic and n^+ layers, and an a-SiC:H p^+ layers; in the present work the a-Si:H cells have microcrystalline (not amorphous) p^+ layers.

We present measurements of the wavelength-dependence of the electroabsorption intercept V_0 in Fig. 2 for a variety of a-Si:H based diodes. A quantitative interpretation for these measurements will be given shortly. Here we note primarily that the interpretation of the wavelength-dependence as a heterostructure effect is reasonably consistent with the measurements on a-Si:H *nim* Schottky barrier diodes. If the wavelength-dependence is to be associated with voltage drops in a p^+ material which is dissimilar to the intrinsic layer, then one expects a much reduced effect in a Schottky barrier in which the p^+ layer is replaced by a metal. Within the metal the potential drops should be insignificant. As can be seen in the

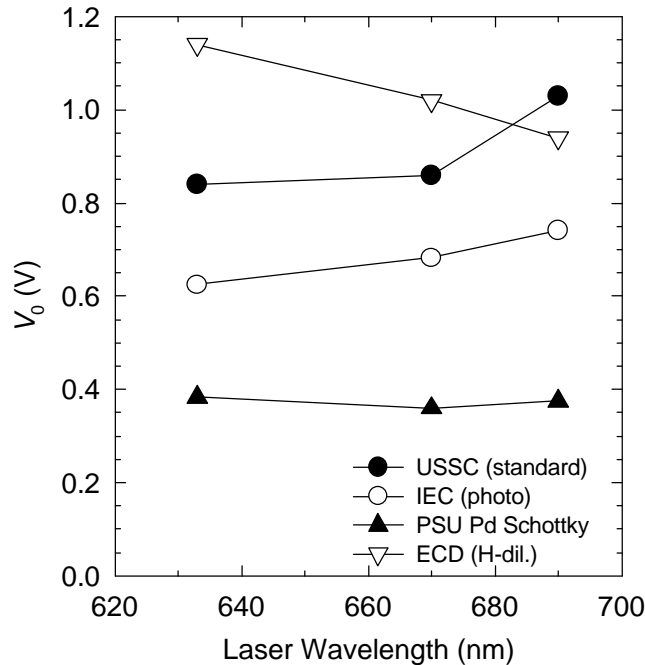


Fig. 2: Wavelength dependence of the electroabsorption parameter V_0 for four different types of a-Si:H based diode structure. In the simplest model V_0 is wavelength-independent, and is identified as the built-in potential. All samples have a-Si:H n^+ layers; all save the ECD sample have conventional a-Si:H intrinsic layers absorbers; the ECD had a high hydrogen dilution absorber. The USSC and ECD diodes had microcrystalline Si p^+ layers; the IEC sample has an a-SiC p^+ layer. Note that the wavelength-dependence is weakest for the Schottky barrier diode with no p^+ layer, suggesting that the wavelength dependence is associated with the varying p^+ layers.

figure, the Schottky barrier structure shows a much reduced wavelength-dependence.

More generally, the “slope” of the wavelength dependence is determined by a competition between the electroabsorption spectra in the p^+ and intrinsic layers. Very roughly speaking, when the p^+ layer has a significantly larger bandgap than the i layer, there is a tendency towards larger values for V_0 for longer wavelengths, where the contribution of the p^+ layer becomes less important. As the i layer bandgap is widened, or the p^+ layer bandgap narrowed, the reverse effect occurs, as for the strongly hydrogen diluted intrinsic layer in Fig. 1. We note that quite similar ideas were used recently by Campbell, *et al* (1995), to interpret electroabsorption measurements on electroluminescent organic heterostructure diodes.

This heterostructure effect undermines efforts to measure V_{bi} quantitatively using electroabsorption. Here we report on a procedure which we believe resolves this difficulty for a-Si:H based solar cells and related devices. We apply the procedure to two types of *nip* solar cells having similar n^+ and p^+ layers, but differing a-Si:H intrinsic layers. In the simplest possible picture the built-in potential is determined by the difference in the Fermi levels of the n^+ and p^+ layers, and should be independent of the intrinsic layer; our estimate of V_{bi} increased from 0.98 to 1.25 V when the intrinsic layer was plasma-deposited using strong hydrogen dilution.

Summary of Heterostructure Model for Electroabsorption

We first describe the model we use for electroabsorption in a *pin* solar cell with a-Si:H n^+ and intrinsic layers and a microcrystalline p^+ layer. In the upper portion of Fig. 3 we show a schematic illustration of the amplitude of the sinusoidally modulated electric field dE . As illustrated, we assumed that this modulation field is uniform across the intrinsic layer, and that it extends only across a depletion zone of the p^+ layer. We also simplified the analysis by neglecting potential drops within the n^+ layer of the cell.

The lower portion of Fig. 3 illustrates the steady-state profile of the conduction band and valence bandedges E_c and E_v ; only the solid black curves are important at present. This figure indicates the band-bending eV_p and eV_i in the p^+ and intrinsic layers, respectively. The built-in potential is defined as

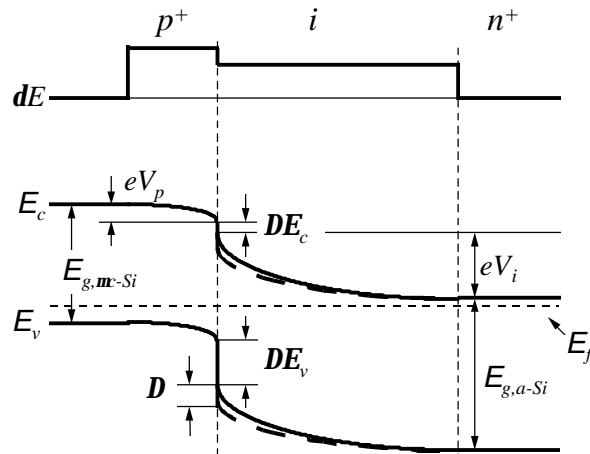


Fig. 3. dE is the amplitude of the modulated electric field across a *pin* solar cell with a microcrystalline p^+ layer. The lower portion indicates the conduction and valence bandedges E_c and E_v across the cell, including band bending in the p^+ and intrinsic layers, band offsets, and an interface dipole Δ .

$V_{bi} = V_p + V_i$. We discuss further details of this figure subsequently.

The electric field dependent absorption in disordered materials is typically quadratic in field $\mathbf{a}(\mathbf{I}, E) = \mathbf{a}^0(\mathbf{I}) + \mathbf{a}''(\mathbf{I})E^2$; \mathbf{a}'' is the *electroabsorption coefficient* of the material. For a sinusoidal modulation of amplitude dV , there will be corresponding transmittance modulations dT_{1f} and dT_{2f} at the fundamental and the second harmonic of the modulation frequency, respectively. We measure these signals as a function of a reverse bias potential V across the cell. Reverse-biasing the cell also increases the width of the depletion zone within the p^+ layer, leading to a decrease in the capacitance $C(V)$ of the cell.

The electroabsorption signals dT_{1f} and dT_{2f} can be obtained from analysis of this model; the derivations are given elsewhere. The second-harmonic signal is particularly important in the present, 2-layer system:

$$\frac{dT_{2f}/T}{(C(V)dV)^2} = \frac{(\mathbf{a}_p''(\mathbf{I})/\mathbf{e}_p)}{2\mathbf{e}_0 C(V)} + \frac{(\mathbf{a}_i''(\mathbf{I})/\mathbf{e}_i - \mathbf{a}_p''(\mathbf{I})/\mathbf{e}_p)}{2\mathbf{e}_0(\mathbf{e}_i\mathbf{e}_0/d_i)} \quad (1)$$

d_i is the thickness of the cell's intrinsic layer; \mathbf{e}_i and \mathbf{e}_p are the dielectric constants of the intrinsic and p^+ layers, respectively. $C(V)$ refers to the area-normalized capacitance measured at the fundamental modulation frequency. Note that a linear regression of the normalized second harmonic signal against the reciprocal capacitance of the cell yields electroabsorption properties of *both* the p^+ layer ($\mathbf{a}_p''/\mathbf{e}_p$) and of the intrinsic layer ($\mathbf{a}_i''/\mathbf{e}_i$).

Once these coefficients are known, the built-in potential in the cell can be obtained using the following expression for normalized fundamental signal:

$$\frac{dT_{1f}/T}{C(V)dV} = -\frac{2\mathbf{a}_i''(\mathbf{I})}{\mathbf{e}_i\mathbf{e}_0} \left\{ (V - V_{bi}) + V_p \left(\frac{\mathbf{a}_p''(\mathbf{I})/\mathbf{e}_p}{\mathbf{a}_i''(\mathbf{I})/\mathbf{e}_i} - 1 \right) \right\} \quad (2)$$

Sample Codes and Notes	i-layer thickness	Voc (V)	“Vbi” (V)	Jsc (mA/cm ²)	FF
HH (treated) USSC/8386#22	0.25	1.039	1.22	8.96	.761
HH (untreated) USSC/8387#22	0.25	1.033	1.17	9.35	.744
LH (treated) USSC/8389#23	0.25	0.957	1.03	10.86	.746
LH (untreated) USSC/8390#22	0.25	0.950	1.02	11.43	.734
HH ECD/LL825	0.5	1.02	1.25		
LH USSC/RF3240	0.5	0.94	0.98		

Table 1: Solar cells specifications used for V_{bi} measurements from United Solar Systems Corp. and from Energy Conversion Devices, Inc..

We note that these expressions neglect thin-film interference effects in the films as well as “true” electroreflectance effects (due to the electric-field dependent refractive index of the films); we do not believe that incorporation of these corrections would significantly alter our conclusions.

Experimental Results on Cells with Microcrystalline p Layers

In the present work we present measurements on six cells deposited in the sequence *nip*. Three cells (denoted “standard” or LH) has a conventional plasma-deposited a-Si:H intrinsic layer; three additional cells (denoted “strong H dilution” or HH) have an intrinsic layer deposited using substantial hydrogen dilution of the silane feedstock gas. All cells have a-Si:H n^+ layers and “microcrystalline” (μ c-Si:H) p^+ layers. The properties of the various samples, as well as our estimates for the built-in potentials, are presented in the Table below.[EAS1]

In Fig. 4 we have shown the measurements of the second harmonic electroabsorption modulation as a function of capacitance for one specimen. The data are generated using the same 50 kHz fundamental modulation frequency and reverse bias range as for Fig. 1. The parameter ratios a_p''/e_p and a_i''/e_i are obtained as linear regression parameters from eq. (1). We present the fitting results for the two thicker cells in Fig. 5, representing the behavior of “low dilution” and for “high-dilution” cells.

The standard and strongly hydrogen-diluted cells yield quite different spectra a_i''/e_i for the intrinsic layers.[EAS2] The results on the standard intrinsic layer agree reasonably well with prior work on a-Si:H. The results for the hydrogen-diluted intrinsic layer presumably reflect the increased bandgap for this layer. The electroabsorption spectra of the microcrystalline p^+ layers in the two cells are similar, as would be expected given that these layers are nominally identical. It is nonetheless remarkable that this result emerged -- considering the substantial differences in the magnitudes and wavelength dependence of the raw electroabsorption signals. The results suggest that the approximations in our heterostructure model are acceptable.

We estimated the built-in potentials in these two cells using the following procedure. We first plotted

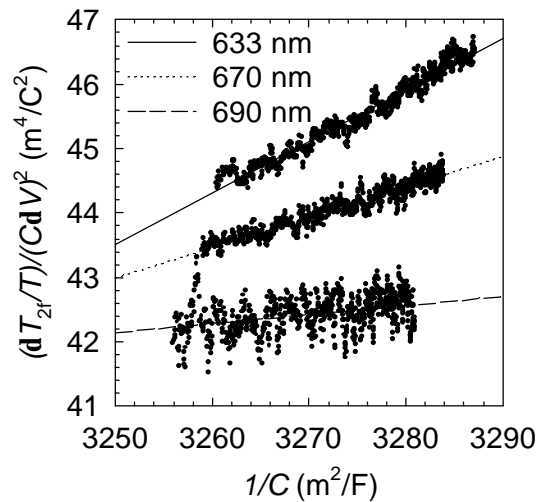


Fig. 4. Plot of the normalized, second harmonic electroabsorption signal dT_{2f} for three different wavelengths as a function of reciprocal capacitance in the standard cell; the data are generated by varying the reverse bias across the cell.

$(dT_{1f}/T)/(C(V)dV)$ as a function of bias voltage in order to obtain the voltage-axis intercept V_0 .

Representative measurements were presented in Fig. 1. V_0 depends slightly upon laser intensity, most likely due to photocharge stored in the samples. In Fig. 5, we have plotted V_0 for low intensities parametrically against the wavelength-dependent ratio $(a_p''/e_p)/(a_i''/e_i)$ (as obtained from Fig. 4). When this ratio is unity, the electroabsorption properties of the p^+ and intrinsic layers are the same. As a consequence, the value of the intercept interpolated for this value can be associated with the built-in potential (by the straightforward single-layer analysis). This qualitative argument is confirmed by equation (2).

As indicated in Fig. 5, we find $V_{bi} = 0.98$ V for the cell with the standard intrinsic layer, and $V_{bi} = 1.25$ V for the cell with the strong hydrogen dilution intrinsic layer. The result for the cell with a standard intrinsic layer and a microcrystalline p is similar to electroabsorption estimates of V_{bi} for cells with an a-SiC:H p layer. As can be seen in the Table above, estimates of V_{bi} for additional cells with smaller intrinsic layer thickness, but otherwise similar materials, are quite consistent with these conclusions. Some of these thinner cells also used an "interface treatment," which very slightly increased V_{oc} and V_{bi} .

Interface Dipole Hypothesis

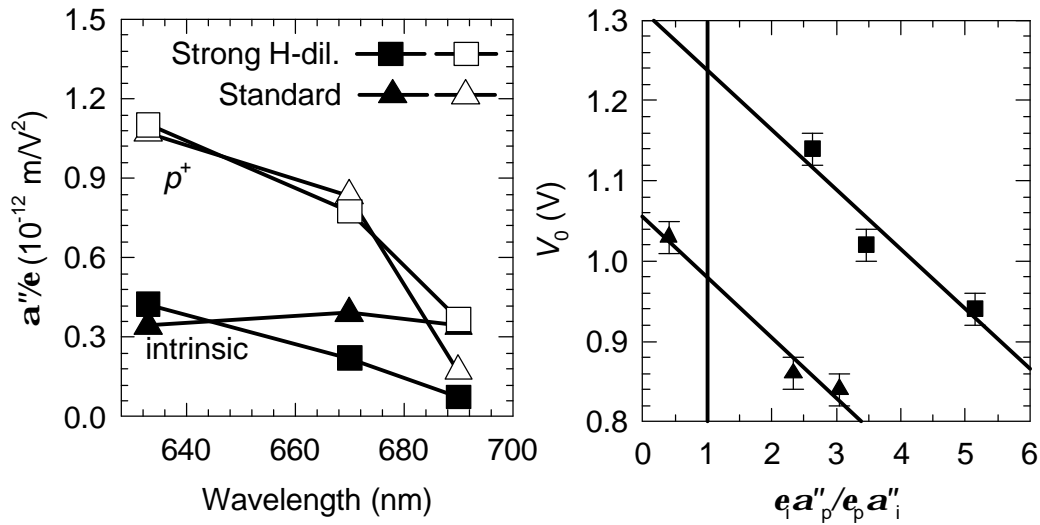


Fig. 5. (left) Electroabsorption coefficients a_i'' and a_p'' as a function of wavelength obtained for a-Si:H and for $\mu\text{c-Si:H:B}$ respectively obtained in two types of cell (with standard and strongly H-diluted intrinsic layers). (right) Plot of the voltage-axis intercepts V_0 of first-harmonic electroabsorption measurements (obtained at three wavelengths) vs. the corresponding ratios of electroabsorption parameters $(a_p''/e_p)/(a_i''/e_i)$. The same two types of cells were used; the error bars indicate the standard deviation in V_0 for differing cells on the same substrate. The built-in potential is V_0 for $(a_p''/e_p)/(a_i''/e_i) = 1$ (cf. vertical line).

The increase in V_{bi} for the strong-hydrogen dilution cell was surprising to us, since it is often assumed that the built-in potential in *pin* diodes should be determined by the Fermi levels of the n^+ and p^+ layers, and should be unaffected by the intrinsic layer interposed between them. This argument of course neglects the possible role of interfaces. We therefore speculate that our measurements are evidence for a significant *interface dipole* between the p^+ and intrinsic layers of a-Si:H based solar cells. By definition, such a dipole consists of compensating positive and negative electric charges separated by a distance comparable to the carriers' tunneling radii. We illustrated the effect of an interface dipole \mathbf{D} in Fig. 3. The solid curves represent the band-bending without the dipole, and shows the effects of the conduction and valence band offsets DE_c and DE_v between the p^+ and intrinsic layer materials. The dashed curves include an interface dipole which reduces the band-bending and hence V_{bi} , increasing the apparent size of both band offsets.

The microscopic nature of such interface dipoles is mysterious, although they have been invoked for nearly 50 years in the context of the built-in potentials in Schottky barrier diodes on crystalline semiconductors and are included in textbook treatments of solar cell device physics. Sizable interface dipole effects (up to 0.7 eV) have been inferred in photoemission studies of the band offsets at the a-Si:H/a-Si_{1-x}C_x:H interface (Fang and Ley, 1989)

For the cells we have studied, it may be that a decrease in interface dipoles for the strongly H-diluted cell is the primary cause for the increase of about 0.1 V in its open-circuit voltage V_{OC} *vis a vis* the standard cell; the possibility is an alternative to attributing the increase in V_{OC} to an increase in the energy gap of the intrinsic layer. The interface dipole hypothesis also leads to some interesting suggestions beyond the electroabsorption measurements. For example, varying interface dipoles offers a rational explanation for the apparently contradictory estimates of band offsets from two independent internal photoemission experiments on c-Si/a-Si:H interfaces; one reported that the offset at the valence band was negligible, and the other reported the conduction band offset as negligible (Mimura and Hatanaka, 1987; Cuniot and Marfaing, 1988). Finally, we speculate that part of the success of "buffer layers" at the p^+/i interface in increasing the open-circuit voltage V_{oc} in some a-Si:H based solar cells is due to modification of interface dipoles.

Since this work was completed, Nuruddin and Abelson (1998) have done Kelvin probe measurements at the interface between p^+ a-SiC:H and intrinsic a-Si:H as deposited by reactive magnetron sputtering. They report the existence of a 0.02 V interface dipole layer -- too small to be of significance in reducing the built-in potential. This experiment should not, in our view, be considered as conclusive evidence *against* significant dipoles effects, but it emphasizes that the dipole hypothesis should be considered provisional until better confirmed.

Heterostructure Model for Electroabsorption: Details

In this section we present a brief derivation of equations (1) and (2) given earlier. We only consider transmittance mode EA measurements; the extension to reflection mode (in which the illumination is reflected from a back-reflector and passes out through the top of the device) is straightforward but tedious.

As is well-known, the absorption coefficient in semiconductors is affected by the electrical field (E) inside the material and the wavelength (λ) of the incident light. Considering the symmetry of electroabsorption, only even order terms survive, so the lowest order expansion is:

$$\mathbf{a}(\mathbf{l}, E) = \mathbf{a}^0(\mathbf{l}) + \mathbf{a}''(\mathbf{l})E^2. \quad (3)$$

We term $\mathbf{a}''(\mathbf{I})$ the electroabsorption coefficient. In modulated electroabsorption measurements, a DC voltage V_{dc} is modulated by a high frequency AC voltage V_{ac} . For sufficiently high frequencies the electric field can be written:

$$E(x, t) = E_{dc}(x) + E_{bi}(x) + E_{ac} \sin \omega t ; \quad (4)$$

ω is the angular frequency of the modulation, and x, t for position and time respectively. Although the DC and built-in fields are position dependent, we have assumed that the modulated field is uniform (corresponding to the use of a large modulation frequency). The electric-field dependent transmittance

through a homogeneous layer of thickness d may be written $T(E) = T_0 \exp\left(-\int_0^d \mathbf{a}''(\mathbf{I}) E^2 dx\right)$; where

$T_0 = I_0 e^{-\mathbf{a}^0(\mathbf{I})d}$. Assuming that the electroabsorption is weak, we expand the exponential $e^{-y} \approx 1 - y$, obtaining:

$$T = T_0 \left\{ 1 - \int_0^d \mathbf{a}''(\mathbf{I}) \left[(E_{dc} + E_{bi})^2 + \frac{E_{ac}^2}{2} + 2(E_{dc} + E_{bi})E_{ac} \sin \omega t - \frac{1}{2} E_{ac}^2 \cos 2\omega t \right] dx \right\} \quad (5)$$

So the normalized first harmonic signal is

$$\frac{dT_{1f}}{T} = -\int_0^d \mathbf{a}''(\mathbf{I}) 2(E_{dc} + E_{bi})E_{ac} dx , \quad (6)$$

and the second harmonic signal is:

$$\frac{dT_{2f}}{T} = \frac{1}{2} \int_0^d \mathbf{a}''(\mathbf{I}) E_{ac}^2 dx . \quad (7)$$

If only a single intrinsic layer is involved in electroabsorption, we can re-express eq. (6) in terms of the capacitance C at the modulation frequency and the modulation voltage V_{ac} . We obtain:

$$\frac{dT_{1f}}{T} \frac{\epsilon_i \epsilon_0 A}{2V_{ac} C} = -\mathbf{a}_i''(\mathbf{I}) (V_{dc} + V_{bi}) ; \quad (8)$$

where ϵ_i indicates the dielectric constant of the layer. As expected, the voltage intercept of the signal is the built-in potential; the second harmonic signal is independent of the DC potential:

$$\frac{dT_{2f}}{T} = \frac{1}{2} \mathbf{a}_i''(\mathbf{I}) \frac{V_{ac}^2}{d_i} . \quad (9)$$

To extend this approach to include electroabsorption both from the p^+ and intrinsic layer, we use the approximation of a depletion zone in the p^+ layer of width d_p , as indicated in Fig. 3. As the reverse bias on the structure increases, the space charge and potential drop V_{dc}^p in the p^+ layer increases as illustrated (for V_{dc}). Increasing reverse bias also increases the “depletion zone” width d_p which is probed by high-frequency measurements. In this model the capacitance is dependent (slightly) upon reverse bias; considering the differences of dielectric constant of two layers and the continuity of electrical displacement vector at the p/i interface, d_p , can be expressed in terms of the capacitance [EAS3] C per unit area as:

$$d_p = \frac{\mathbf{e}_p \mathbf{e}_0}{C} - \frac{\mathbf{e}_p}{\mathbf{e}_i} d_i. \quad (10)$$

The I_f signal now becomes:

$$\frac{dT_{1f}/T}{C(V)dV} = -\frac{2\mathbf{a}_i''(I)}{\mathbf{e}_i \mathbf{e}_0} \left\{ (V - V_{bi}) + V_p \left(\frac{\mathbf{a}_p''(I)/\mathbf{e}_p}{\mathbf{a}_i''(I)/\mathbf{e}_i} - 1 \right) \right\}. \quad (11)$$

where we have separated the built-in potential V_{bi} into its components V_p and V_i across the p^+ and intrinsic layers, respectively. We have also redefined V_{ac} as dV to re-establish consistency with our earlier equations 1 and 2.

Note that when the “electroabsorption ratio” $\mathbf{e}_i \mathbf{a}_p''(I)/\mathbf{e}_p \mathbf{a}_i''(I)$ is unity, the standard analysis of EA measurements yields the correct $V_{bi} = V_{bi}^i + V_{bi}^p$; this was previously suggested by Wang, *et al* (1994) on purely physical grounds, since the 2 distinct layers then have identical electroabsorption properties.

The difficulty has been to find a procedure for ascertaining this electroabsorption ratio. We have found that the second harmonic ($2f$) measurements can be used to do this. From eq.(9) and eq.(10), the $2f$ signal can be expressed as:

$$\frac{dT_{2f}/T}{(C(V)dV)^2} = \frac{(\mathbf{a}_p''(I)/\mathbf{e}_p)}{2\mathbf{e}_0 C(V)} + \frac{(\mathbf{a}_i''(I)/\mathbf{e}_i - \mathbf{a}_p''(I)/\mathbf{e}_p)}{2\mathbf{e}_0 (\mathbf{e}_i \mathbf{e}_0 / d_i)}. \quad (12)$$

On the right side of Eq. (10), only the capacitance C changes with V_{dc} .

The importance of this expression is that, unlike eq. (9), we do not need to know the division of the electric potential between the p^+ and intrinsic layers in order to use it. A fitting of the measurements to the voltage-dependent capacitance yields both \mathbf{a}_p'' and \mathbf{a}_i'' as fitting parameters.

Polarized Electroabsorption Spectra and Light-Soaking of Solar Cells Based on Hydrogenated Amorphous Silicon

Introduction

About ten years ago Weiser, Dersch, and Thomas (1988) reported the *polarized electroabsorption effect* for the interband optical absorption of amorphous selenium and hydrogenated amorphous silicon (a-Si:H). In particular they found that the electroabsorption (EA) spectrum (the electric-field dependent portion of the absorption itself) depended significantly upon the angle between the polarization vector of the optical beam and the external electric field applied to the material. They interpreted the effect in terms of the nature of electronic states near mobility edges (the level energy separating localized and extended states near the conduction or valence bandedges).

Other scientists have significantly extended this initial work. Okamoto, *et al* (1991) and Tsutsumi, *et al* (1994) proposed that the polarized electroabsorption effect is well correlated with the fundamental mobilities of electrons and holes. Most recently Shimizu, *et al* (1997) and also Hata, *et al* (1997) reported that the polarization dependence of electroabsorption is nearly doubled in magnitude by “light-soaking” of a-Si:H, which is a new type of *Staebler-Wronski effect* (Staebler and Wronski, 1977). These measurements suggest the highly significant conclusion that light-soaking substantially changes the electronic structure of a-Si:H – especially in the mobility-edge regions. The preponderance of work on the Staebler-Wronski effect has emphasized point defect generation during light soaking as opposed to more broadly based changes to the material itself.

The electroabsorption measurements cited above were performed on simple thin-film specimens. The external electric potential difference was applied between two electrodes separated by a small gap; the optical beam passes through this gap. One potential difficulty with this “coplanar electrode” geometry is that the measurements are affected by interfacial fields and by non-uniformity of the applied field. In particular, Mescheder and Weiser (1985) have documented a strong nonuniformity of the electroabsorption signal across the electrode gap for a-Si:H, reporting that the signal close to the electrodes was about one order of magnitude higher than the signal from the middle of the gap. While this nonuniformity clearly presents a quantitative difficulty (Zelikson, *et al*, 1996), several authors have argued that the electroabsorption spectra, and the relative magnitudes for the polarization effect, should be unaffected by it.

In this paper we present electroabsorption measurements using a “sandwich” electrode geometry which, we believe, greatly reduces these uncertainties. We confirm the existence of the polarized electroabsorption effect, and indeed we conclude that the polarization dependence is substantially larger, and hence of even greater interest, than previously reported. On the other hand, we did not reproduce the light-soaking effect found in the coplanar geometry. An interesting byproduct of the current measurements is an estimate of the change in the built-in potential of our a-Si:H based solar cells due to light-soaking; this effect was also unmeasurably small (<0.03 V change). At the conclusion of this paper, we speculate as to the origins for the Mescheder-Weiser effect and for the differing conclusions from experiments in the two geometries.

Polarized Electroabsorption Techniques for Solar Cells

We first describe our experimental configuration for polarized EA measurements. As shown in Fig. 6, we use *p-i-n* diodes for the measurements; both the internal and external electric fields are normal to the interfaces as illustrated. The incident optical beam is at near-grazing incidence. For the incident *s*-polarization the optical polarization vector and the macroscopic electric field are perpendicular; for incident *p*-polarization the optical polarization has a component which is parallel to the electric field.

The dependence of the electroabsorption spectrum $\Delta\mathbf{a}(h\mathbf{n},\mathbf{q})$ upon the optical polarization can be expressed as

$$\Delta\mathbf{a}(h\mathbf{n},\mathbf{q}) = \Delta\mathbf{a}_i(h\mathbf{n}) + \Delta\mathbf{a}_a(h\mathbf{n})\cos^2\mathbf{q}, \quad (1)$$

where \mathbf{q} is the angle between the optical polarization vector and the field, and $\Delta\mathbf{a}_i(h\mathbf{n})$ and $\Delta\mathbf{a}_a(h\mathbf{n})$ are defined as the isotropic and anisotropic spectra, respectively. The spectra can be related to the electroabsorption measured with *s* and *p* polarizations:

$$\Delta \mathbf{a}_i(h\nu) = \Delta \mathbf{a}_s(h\nu), \quad (2a)$$

$$\Delta \mathbf{a}_a(h\nu) = (\Delta \mathbf{a}_p(h\nu) - \Delta \mathbf{a}_s(h\nu)) / \sin^2 r = (\Delta \mathbf{a}_p(h\nu) - \Delta \mathbf{a}_s(h\nu)) / \left(\frac{\sin i}{n} \right)^2, \quad [4] \quad (2b)$$

where the subscripts s and p denote the polarization of the beam, i denotes the incidence angle in air, r denotes the angle of propagation inside the Si, and n is the index of refraction of the intrinsic layer.

The samples employed in this experiment are p - i - n structure solar cells. The United Solar sample was deposited onto a glass substrate coated with a thin film of Cr using the sequence: P-doped a-Si:H n^+ layer, 0.4 μm intrinsic a-Si:H layer, and an about 10 nm B-doped microcrystalline silicon ($\mu\text{c-Si}$) p^+ layer. The Solarex sample was deposited onto a glass substrate coated with a textured conducting oxide in the sequence: B-doped a-SiC p^+ layer, intrinsic layer, and P-doped a-Si:H n^+ layer. It is very convenient for the measurements that both top and bottom electrodes are semitransparent, which permits direct optical transmittance measurements.

We used lasers and monochromatic illuminators as illumination sources. These were unpolarized sources, and we polarized their light using rotating Polaroids. The transmitted beam was detected using a Si photodiode or a photomultiplier. Light soaking was done using a helium-neon laser (633 nm) under open-circuit condition; we were careful to assure that the illumination intensity during an electroabsorption measurement did not change the light-soaking state significantly. The external reverse-bias potential across the diode was modulated at 50 kHz field, which is sufficiently rapid that the external electric field across the intrinsic layer is essentially uniform. We estimate the electroabsorption $\Delta \mathbf{a}$ from the modulation ΔT of the transmittance:

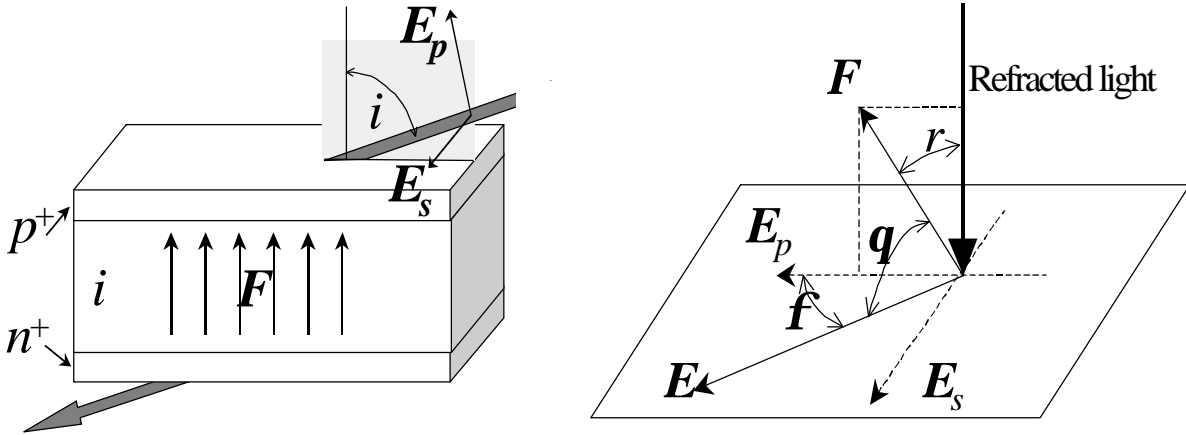


Fig. 6: Illustration of grazing incidence angle measurements of polarized electroabsorption. (left) The incident beam (shaded arrow) is refracted and transmitted as it passes through a p - i - n solar cell; F denotes the macroscopic electric field, E_p and E_s denote the optical polarization. (right) Definitions of the various angles involved in analyzing the experiment: the refraction angle r , the polarization angle f , and the angle q between the external and polarization fields.

$$(\Delta a)l \approx (\Delta T/T), \quad (3)$$

where l is the length of optical path of the beam in the sample. For the present experiments one aspect of this equation should be noted. The transmittance T depends significantly upon polarization at non-normal incidence – but the electroabsorption coefficient calculated according to eq. (3) is independent of this effect. We do neglect thin-film interference effects in our analysis; Weiser, *et al* (1988) have discussed this simplification at some length in previous work.

We briefly discuss the scaling of the electroabsorption with electric field. In a-Si:H, electroabsorption is quite accurately proportional to the square of the electric field for fields up to at least 10^5 V/cm in a-Si:H (Weiser, Dersch, and Thomas, 1988; Tsutsumi, et al, 1994; Jiang, et al, 1996). This fact leads to a definition for the fundamental electroabsorption coefficient α'' in terms of the measured

electroabsorption $\Delta a = \alpha'' F^2$, where F is the electric field. Experimentally, the application of this definition is not straightforward; for the present “sandwich” electrode arrangement, we simultaneously measure both the built-in potential across the $p-i-n$ diode as well as the fundamental coefficient α'' using procedures we have reported previously (Jiang, et al, 1996); the estimates are nearly insensitive to the details of the static internal field profile across the structure.

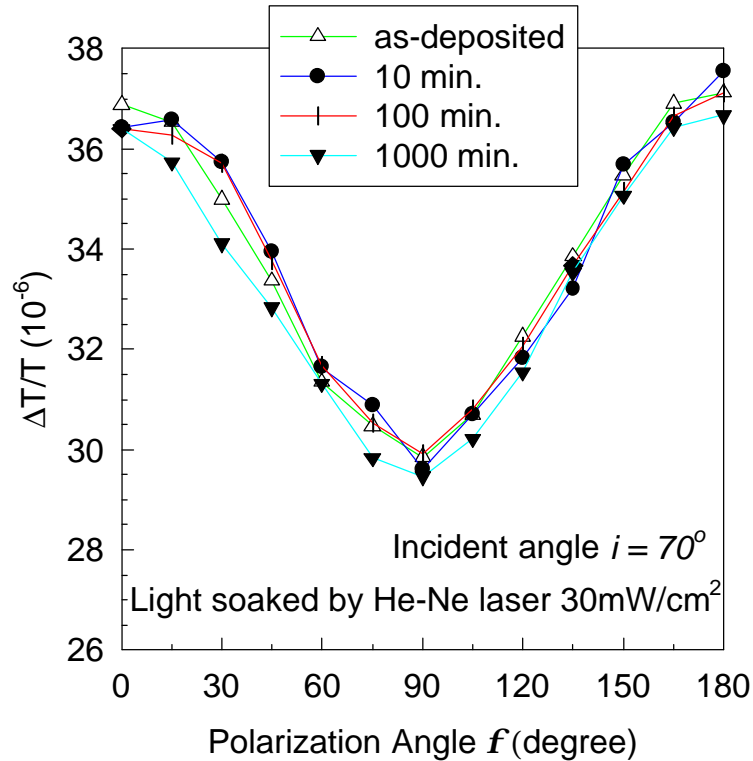


Fig. 7: Measurements of the electric-potential modulation ΔT for the transmittance T in a United Solar specimen. $\Delta T/T$ is plotted as a function of polarization of the incident beam. Curves are shown for four different light-soaking states of the cell.

Results

We first illustrate how we used “sandwich” electrodes to measure the polarized electroabsorption effect. In Fig. 7 we have plotted the transmittance modulation $\Delta T/T$ for a helium-neon laser (633 nm) measured as a function of the polarization angle θ (cf. Fig. 6). Results for four different light soaking states are shown. In all states we find a clearly measurable effect of polarization; the relatively small magnitude was expected, since even at grazing incidence ($i = 90^\circ$) the polarization vector of the p -polarized refracted beam has only a modest component (28.5%) of its magnitude which is parallel to the internal field \mathbf{F} .

In Fig. 8(a) we have presented the isotropic and anisotropic electroabsorption spectra calculated from the modulated transmittance according to eq. (2). We measured essentially the same spectra for a United Solar sample.

In Fig. 8(b) we compare the EA spectra of as-deposited state and a light soaked state for the Solarex specimen. Consistent with Fig. 2 for United Solar specimen, we find no statistically significant difference. In both cases we used fairly weak illumination (30 mW/cm^2) to light-soak the samples; we chose this intensity for consistency with the previous measurements with coplanar electrodes, for which

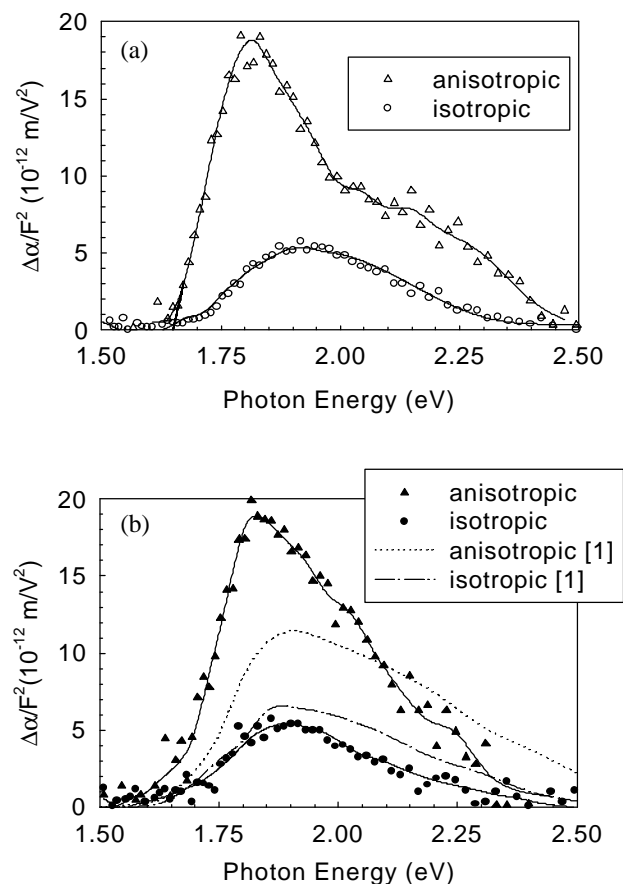


Fig. 8: Polarized electroabsorption spectra for a-Si:H. (a) Measurements for the as-deposited state of a Solarex specimen; solid lines are a running average of three wavelength samples. (b) Symbols and solid lines show spectra for the Solarex specimen after 1 hour light soaking (30 mW/cm^2) with a He-Ne laser (633nm). Dotted and dashed lines are the measurements reported by Weiser, *et al* (1988).

only short exposures at 30 mW/cm^2 were required to observe the light-soaking effect on electroabsorption. This level of light-soaking did increase the photocurrent response of the diode in the infrared (1.0 eV) by 2.5 times; this infrared effect may be attributed to the creation of midgap defects by light-soaking. An interesting by-product of the present measurements is an electroabsorption estimate of the built-in potential V_{bi} of the solar cell (Jiang, et al, 1996); this parameter changed less than 0.03 V as a result of light-soaking.

A more sensitive test for light-soaking effects is to plot the ratio of the isotropic and anisotropic electroabsorption during light-soaking. This is done for two samples in Fig. 9; we find no effect to within a sensitivity of about 3%.

In summary, we find that the isotropic electroabsorption spectra are fairly comparable using either coplanar or sandwich electrodes. The anisotropic spectrum estimated using sandwich electrodes is substantially stronger and distinct in shape than the isotropic spectrum, whereas the anisotropic spectrum estimated with coplanar electrodes is relatively similar to the isotropic spectrum and exhibits a light-soaking effect. We suspect that the differences may indicate that the applied electric field in some regions of the coplanar electrode gap is not parallel to the plane of the film, which would account for the reduced contrast between the isotropic and anisotropic spectra with these electrodes. A complete two-dimensional analysis of coplanar electrodes, incorporating non-uniform applied and non-uniform interface fields, is beyond the scope of the present work. We have more confidence in the analysis for sandwich electrodes (Jiang, et al, 1996), where a one-dimensional treatment is possible and where the field modulation (although not the DC field) is arguably uniform.

We therefore presume that the sandwich electrode measurements are the better reflection of fundamental electroabsorption spectra, and that the coplanar measurements are offering unexpected information about the electric field patterns between its electrodes. As has been noted before (Weiser, Dersch, and Thomas, 1988; Okamoto, et al, 1991; Tsutsumi, et al, 1994), these fundamental electroabsorption spectra offer a tantalizing, but obscure, insight into the nature of electronic states near mobility edges. The distinctness of the anisotropic and isotropic spectral shapes, which was not apparent from previous work, does suggest that polarized electroabsorption is reflecting two distinct optical processes.

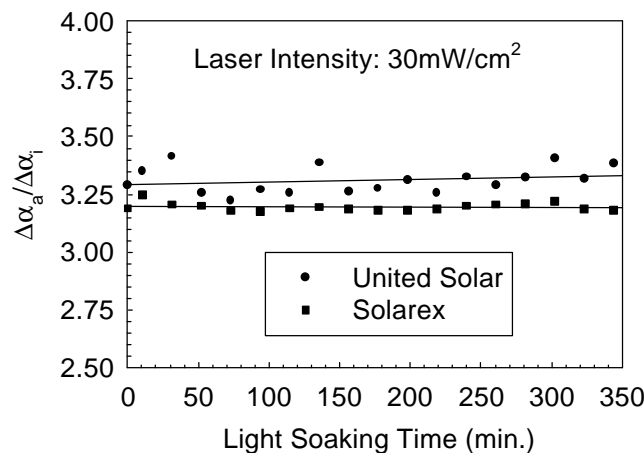


Fig. 9: Anisotropic/isotropic polarization ratio for electroabsorption measured during light-soaking at 30 mW/cm^2 . Measurements are shown for two a-Si:H based *p-i-n* solar cells from different laboratories.

Electroabsorption Spectra of Amorphous and Microcrystalline Silicon

Introduction

Electroabsorption (EA) studies the effect of an applied electric field on the optical absorption of materials. The spectrum differs significantly for the three important classes of semiconductors: direct bandgap, indirect bandgap, and amorphous. For crystalline silicon, an indirect bandgap crystal, Fropa, *et al.* (1966) found weak, sharp features in the electroabsorption spectrum at optical energies corresponding to the sum or difference of the bandgap and an optical phonon energy. Direct bandgap crystals such as CdS have vastly stronger electroabsorption, and a strongly oscillating spectrum above the bandgap (Blossey and Handler, 1972; Shen and Pollak, 1989). Exciton theory has been exploited to explain those rich features in the EA spectra of crystalline materials (Blossey and Handler, 1972; Penchina, 1965; Blossey, 1971). For amorphous silicon, the EA spectrum is a broad band which is much stronger than for crystal silicon, but still much weaker and lacking the oscillatory character of the direct bandgap crystalline spectrum.

Several surprising features of the EA spectra for amorphous solids rule out exciton theory as the origin of electroabsorption (Weiser, Dersch, and Thomas, 1988). The EA signal is always positive, which indicates that external field increases absorption in whole energy range. The exponentially rising tail at the lower energy end of the spectra is the signature of the exponential localized bandtails of amorphous silicon materials. No strong oscillation, which is supposed to be the primary indication of the exciton mechanism, is observed in the EA spectra of amorphous solids.

An important additional distinction between the electroabsorption in amorphous and crystalline materials is the polarization effect discovered in the amorphous solids, but missing from crystals (Gelmont, *et al.*, 1981; Mescheder and Weiser, 1985). Specifically, the electroabsorption strength in amorphous silicon more than doubles as the electric field is rotated from being perpendicular to being parallel to the optical polarization vector. Although the exciton theory used in crystals appears inapplicable to electroabsorption in amorphous solids, no quantitative theory for the effect has emerged.

The differing signatures of electroabsorption in the varying classes of semiconductors suggest that it may be interesting to apply electroabsorption to microcrystalline silicon prepared by plasma deposition from silane/hydrogen mixtures. This type of microcrystalline silicon is a complex, mixed-phase material potentially containing crystallites of varying sizes as well as amorphous silicon (Hapke, *et al.*, 1996); some of the crystallites can be of nanometer scale, and thus are expected to exhibit quantum confinement effects. Microcrystalline silicon is also technologically important, being used in some thin-film silicon solar cells and for flat panel electronics, and improvements in the understanding of the material's properties are thus important in this context also.

In this paper we present our measurements on electroabsorption in a series of microcrystalline silicon samples; to our knowledge, no EA spectra on microcrystalline silicon have been reported by other laboratories. Very beautiful EA spectra for CdS and CdSe nanocrystallites with well-defined size embedded in glasses were recently reported by Cotter, Girdlestone, and Moulding. (1991). They confirmed quantum confinement effect by observing the shift of the absorption edge to higher energy with decreasing particle size, as predicted using exciton theory in finite size crystals (Ren and Dow, 1992; Furukawa and Miyasato, 1988). Photoluminescence and electroluminescence has been reported in nanocrystalline and porous silicon, again with the conclusion that quantum confinement effects dominate the spectrum and its strength (Brus, 1994; Delerue, *et al.*, 1995^[EASSI]).

In this paper we present our experimental results on EA spectra for thin films of microcrystalline silicon. We found that the peak position of EA spectra, which is the indication of bandgap, shifts to higher energy systematically as the nominal crystalline volume fraction (estimated by Raman scattering) increases. We attribute the electroabsorption to interstitial material lying between relatively large (>10 nm) crystals. The polarization effect of EA spectra disappears as the crystalline volume fraction increases. Since the polarization effect is considered a signature of amorphous structure, we conclude that the interstitial material is nanocrystalline, and that the blue-shift of the electroabsorption *vis a vis* bulk, crystalline silicon is due to quantum confinement effects. A corollary of this viewpoint is that the use of Raman scattering to infer that interstitial material is amorphous is invalid; we speculate that the Raman scattering from nanocrystallites is essentially indistinguishable from that of amorphous silicon.

Experiments

Samples

We used two sets of samples in our EA spectra experiments. Our primary focus is on four samples in a series deposited with PECVD from silane/hydrogen mixtures at Forschungszentrum Jülich. Thin films were deposited on glass substrates using the same conditions except that the silane concentration $S = \text{SiH}_4/(\text{SiH}_4 + \text{H}_2)$ of the source gas was varied; decreasing values of S are associated with increasing degrees of microcrystallinity (Carius, et al, 1997). We then used Raman scattering to estimate the volume fraction of the microcrystalline phase following the procedure of Fauchet and Campbell (1988). The Raman spectra for all four samples are shown in Fig. 10, and a summary of sample features is presented in table 1. As shown in the table, we have a consistent trend of reduced amorphous content in the sample series as we reduced the silane concentration during deposition. We evaporated coplanar metal electrodes on top of these films to permit the electroabsorption measurements.

For reference, we also include spectral results on two *pin* diode samples prepared at United Solar Systems Corp.; the intrinsic (undoped) layers in these diodes are amorphous, but the two samples vary in the extent of hydrogen dilution during deposition. Amorphous silicon deposited under higher hydrogen dilution (“HH”) conditions have slightly larger optical bandgaps, as indeed is illustrated by their electroabsorption spectra.

Electromodulation Spectroscopy

We present some details of our measurements on the microcrystalline films with coplanar electrodes. The beam from the monochromator was polarized by the rotating Polaroids and then passes through the

Table 2: The Crystalline Content in Samples from Raman Spectra

Silane concentration	2%	3%	5%	6%
Sample thickness (nm)	357	530	711	750
Deposition rate (Å/s)	0.6	0.97	1.3	1.38
Crystalline content by Raman Scattering	84%	76%	76%	62%

gap between the electrodes. The electric potential across the gap is switched between zero and some positive value corresponding to about 18 kV/cm across the gap.

The transmitted beam is then detected by either a semiconductor diode (Si or InGaAs) or a photomultiplier and appropriate preamplifiers. The DC photocurrent from the detector was recorded using a computer; the modulated detector photocurrent was detected using a two-phase lockin amplifier which responds to first harmonic of the modulation frequency. The two outputs from the lockin were again recorded by a computer.

A stepping motor in the monochromator steps through the whole visible wavelength range; we used a computer to drive the stepping motor, permitting us to record the spectrum of the DC and modulated photocurrents from the detectors. We also used spectral signal averaging: the spectra reported here are actually the average of many spectra recorded fairly rapidly using the computer controlled instrument and then subsequently averaged.

We used 5kHz modulation of the electric potential across the electrode gap. We found that 1kHz modulation, which is used for most amorphous silicon materials previously [Mescheder and Weiser, 1985; Hata, et al, 1997), is not fast enough to make the competing signal from heat effects totally negligible. This difficulty can be traced to the increased conductance of some of the microcrystalline samples *vis a vis* amorphous silicon. The spectra reported here do correspond to a high-frequency asymptote and were in-phase with the voltage modulation -- as expected for true electroabsorption processes.

For this type of flat thin film sample, interference fringes can be severe in the transmittance and (especially) the modulated transmittance spectra. Modulated transmittance measurements are shown in Fig. 11 for one sample. The strong oscillations are mainly due to electric-field induced changes in

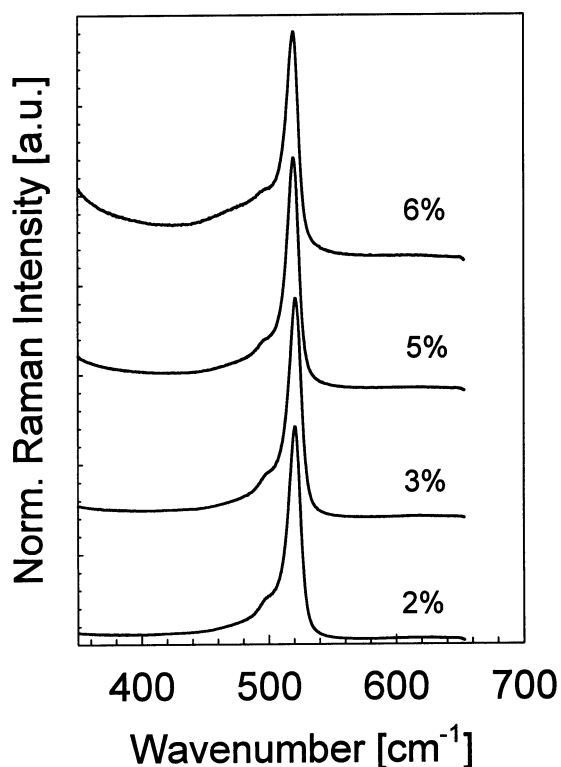


Fig. 10: Raman spectra of four samples deposited with different silane concentration with PECVD.

refractive index; one is essentially looking at an optical-energy (or wavenumber) derivative of the interference fringes in the raw transmittance of the sample. We did not attempt a more serious analysis, but simply take the centerlines of the fringes to estimate the electroabsorption, as shown in Fig. 2.

Our procedure for handling the interference fringes will lead to some systematic errors. We believe these errors are small compared to a second systematic error in thin-film samples uncovered some years ago by Mescheder and Weiser (1985), who showed that electroabsorption signal strength is strongly affected by contact effects and space charge problem in coplanar samples. Presumably the shape of the EA spectra should still be valid, but the magnitude of the electroabsorption can be in error by as much as a factor two. We have discussed this issue at greater length elsewhere (Jiang, et al, 1998).

We take the spectra with light polarization parallel to electric field ($\Delta\mathbf{a}_{//}$) and perpendicular to the field ($\Delta\mathbf{a}_{\perp}$). It is well known that the possibility for polarized transition is proportional to $(\mathbf{P} \cdot \mathbf{E})^2$, where \mathbf{P} stands for dipole and \mathbf{E} denotes polarization vector, so for polarized EA we have the general equation:

$$\Delta\mathbf{a} = \Delta\mathbf{a}_i + \Delta\mathbf{a}_a \cos^2 \mathbf{q}, \quad (1)$$

where \mathbf{q} denotes the angle between polarization and the field, $\Delta\alpha_i$ and $\Delta\alpha_a$ denote the isotropic and anisotropic electroabsorption components respectively. Since the light passes the sample with normal incidence and the field is in the plane, thus $\theta=90^\circ$, then we simply have the isotropic and anisotropic components as follows,

$$\Delta\mathbf{a}_i = \Delta\mathbf{a}_{\perp}, \quad (2)$$

$$\Delta\mathbf{a}_a = \Delta\mathbf{a}_{//} - \Delta\mathbf{a}_{\perp}. \quad (3)$$

The polarization ratio is defined as the ratio of the peak heights of anisotropic and isotropic spectra

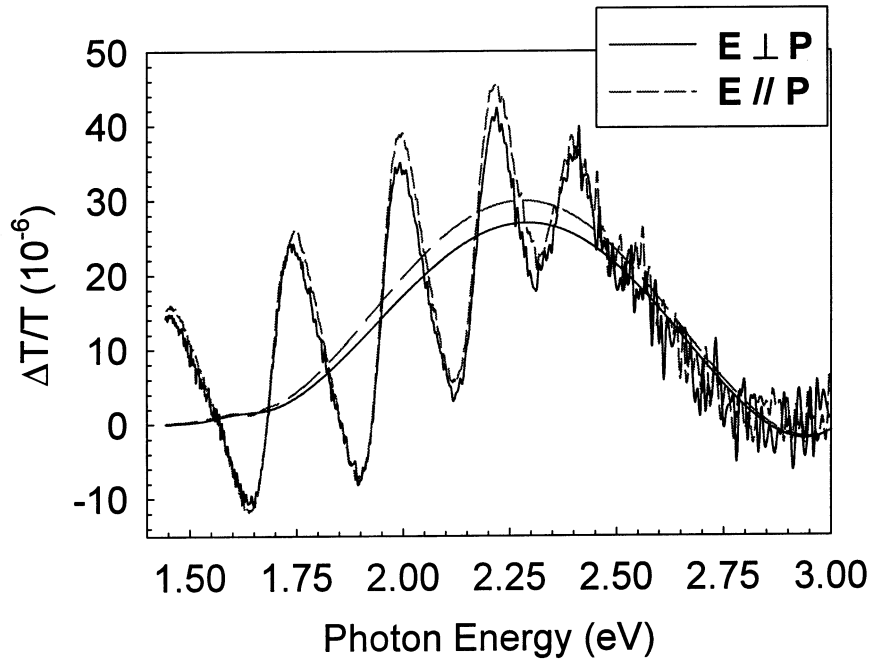


Fig. 11: The experimental electroabsorption spectra of sample made by 3% silane concentration. Guidelines are included in the figure as a simple solution for severe interference fringes. Both spectra for electrical field parallel to and perpendicular to the light beam polarization are shown in the figure.

$$\Delta a_a / \Delta a_i.$$

Results

First, we used unpolarized monochromatic beam as the light source to study the EA spectra of the microcrystalline samples. The results are shown in Fig. 12. In the figure, we also include the results for the two pure amorphous silicon samples for comparison (LH indicates “low hydrogen dilution” during PECVD, and HH indicates high hydrogen dilution); these data correspond to the perpendicular polarization, and thus the magnitudes are not expected to be strictly comparable to those with unpolarized light. Notice that the low-hydrogen-dilution sample shows an EA peak at 1.86 eV, while the high-hydrogen-dilution one has the peak at 1.94 eV; the difference presumably corresponds to the difference in optical bandgaps from standard transmittance measurements.

As is evident in Fig. 12, the EA spectra for the four microcrystalline samples are all broad bands similar in strength to those for amorphous silicon, but substantially blue-shifted in spectral position. . The largest energy shift reaches 0.60 eV, i.e., the peak shifts from 1.86 eV for “garden-variety” amorphous silicon to 2.46 eV for material with a substantial crystalline phase.

We did not observe the sharp peaks and oscillations expected for crystalline silicon near 1.1 eV . This surprised us, since some of the microcrystalline samples primarily consist of fairly large (> 10 nm diameter) c-Si grains. Similar results are found by Woggon et al (1994) on CdS with widely varying crystal size in organic matrix.

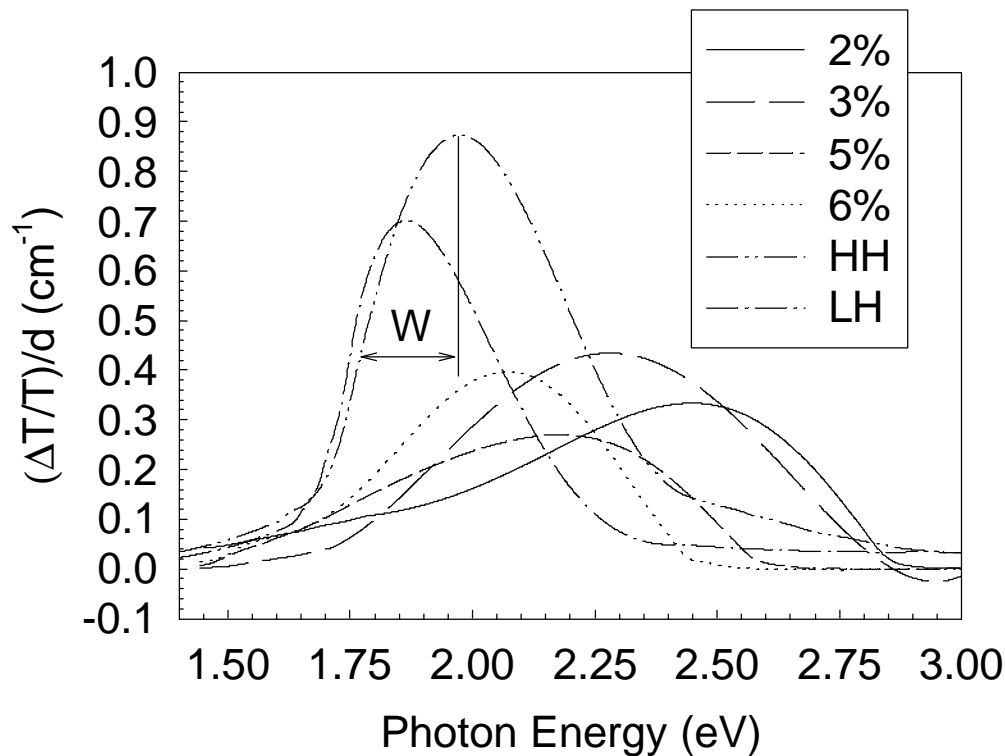


Fig. 12: The electroabsorption spectra of pure amorphous silicon and mixtures of amorphous and microcrystalline silicon.

Another feature of Fig. 12 is that the rising edge of the EA spectra broadens with increasing peak blue-shift (and increasing microcrystallinity). We defined an energy-width W as the decrease in optical energy required for the electroabsorption to fall to half its peak value; this definition is illustrated in Fig. 12. In Fig. 4 we plot W versus the EA peak energy. Obviously, the rising edge width increases dramatically as the bandgap is blue-shifted. We also studied the polarization dependence of the EA spectra. In Fig. 13 we have plotted the ratio of EA with electric field parallel and perpendicular to the applied electric field; the ratios were measured at the peak position of the electroabsorption. As is evident, this ratio declines with the blue-shift and with increasing microcrystallinity.

Discussion

Our principal concern in this section is the electroabsorption bands measured in the microcrystalline silicon samples. It appears unlikely that these bands are related to the larger Si crystallites which are the principal component of these samples; Carius, *et al.* (1997) previously reported that the average grain size of same type of samples with 60% - 80% crystalline content was around 150Å – 250Å. Such crystallites are sufficiently large that we expect them to behave essentially the same as bulk c-Si. The electroabsorption in bulk Si is much weaker than we observe, nor do larger crystallites account for the blue-shift of these bands. We therefore seek an explanation based on relatively strong electroabsorption from the modest fraction of “interstitial” material lying between the larger crystallites.

This interstitial material is also presumably the origin for the “amorphous” component in the Raman spectra, but here we consider both the possibility that the material is amorphous, and also the possibility that it is comprised of small nanocrystals. In fact we favor this latter explanation based on the electroabsorption measurements. If this latter case obtains, it implies that the Raman spectrum misleadingly suggests that the interstitial material is truly non-crystalline. Presumably the Raman spectra of sufficiently fine nanocrystallites are similar to those for non-crystalline silicon – which does seem a possible consequence of the breakdown of crystal momentum conservation in nanometer scale materials.

The explanation for the blue-shift in a nanocrystalline interstitial material is a straightforward application of the idea that quantum confinement in small crystallites blue-shifts the optical absorption: the electroabsorption spectrum is the superposition of the electroabsorption of an inhomogeneous distribution of nanocrystallites. Based on theoretical calculations, the substantial magnitude of the blue-shift requires that these nanocrystallites have dimensions between 1 and 2 nm.

One possible difficulty with this view is that the electroabsorption strength of the interstitial material (following integration over optical energy) is of the same order of magnitude as amorphous silicon – despite the fairly small volume fraction we associate with it. We must conclude that the electroabsorption is at least 2 orders of magnitude larger than that for crystalline silicon (Frova, et al, 1966). Hybertsen (1994) and other authors have calculated the band structure in nanocrystals, and concluded that quantum confinement enhances zero-phonon radiative transitions by several orders of magnitude. These calculations were used in the context of the surprising large photoluminescence efficiency in porous silicon, but a similar enhancement no doubt applies to other aspects of zero-phonon transitions, including electroabsorption.

This argument also makes it clear that the EA spectrum would not be a direct reflection of the bandgap distribution of the nanocrystals, but rather the product of this distribution and the electroabsorption strength of nanocrystals, which apparently increases for smaller nanocrystallites. The reason we obtained different EA spectra for different samples is that the distribution of nanocrystal sizes in the interstitial material is changing.

Finally, consider the polarization dependence of electroabsorption. The discoverers of this effect consider it to be a characteristic signature of an amorphous solids; it has been observed in amorphous silicon, amorphous Se, and other amorphous materials (Weiser, Dersch, and Thomas, 1988), but not in bulk crystalline solids. The collapse of the polarization ratio to near zero strongly suggests that a crystalline material is causing the electroabsorption bands.

For completeness, we briefly describe an alternative model for the interstitial material – which is that it is

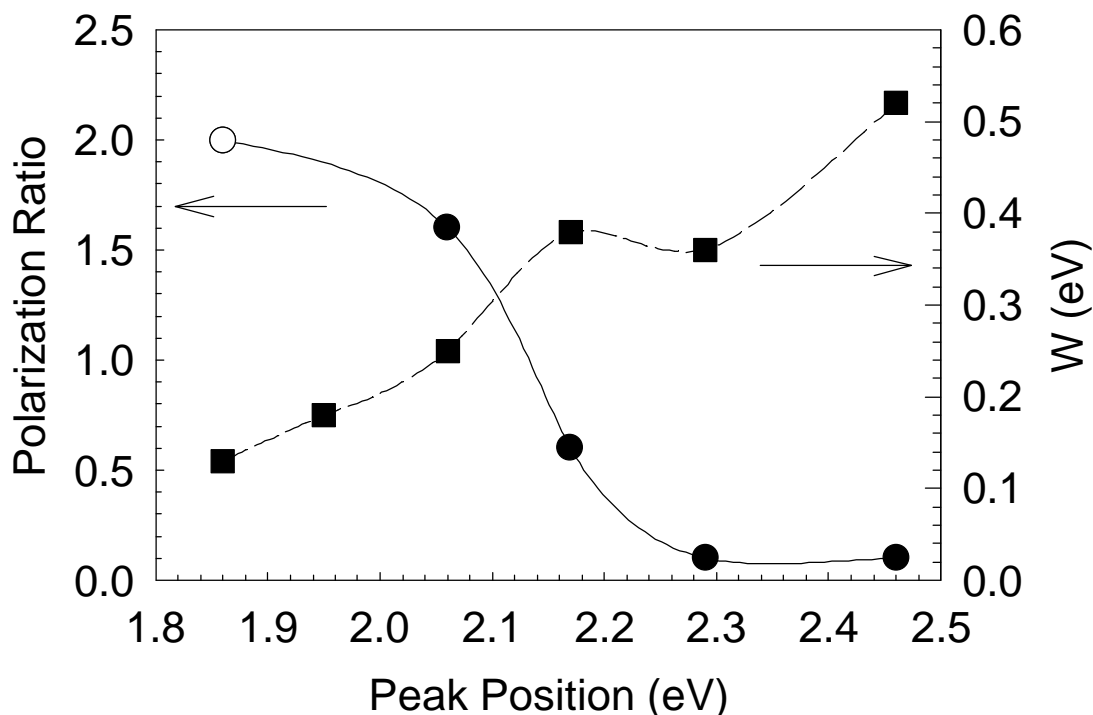


Fig. 13: Polarization ratio and rising edge width W versus the EA peak blue-shift. The empty dot is taken from Penchina (1965) in order to be consistent with the present data obtain by co-planar geometry. Please refer to Jiang, et al (1998) for comparison of co-planar and sandwich electrode geometry.

primarily amorphous. This is the view suggested by Raman scattering, and it also readily accounts for the strength of the electroabsorption. The blue-shift would either be a result of “quantum confinement” effects for the amorphous material, which might exist in nanometer scale domains, or alternatively of increases in the hydrogen content of the amorphous silicon. In any event the hypothetical amorphous interstitial material would need to be quite inhomogeneous to account for the large width of the electroabsorption spectrum. We tend to discount this model because it gives no ready explanation for the decline of the polarization ratio in highly microcrystalline material, and because it leads less naturally to the broad width.

Unusually Large Hole Drift Mobilities in Hydrogenated Amorphous Silicon

Introduction

The low drift mobility of holes is an important limitation to amorphous silicon based materials, and there have been many efforts to find deposition processes which would improve it. The hole mobilities are limited by trapping processes involving the valence bandtail. Remarkably, for the entire class of plasma-deposited amorphous silicon-germanium and amorphous silicon-carbon alloys deposited in “diode” reactors, representing many years of materials research, it has been found that the hole drift mobility remains nearly constant, with a best value of $2 \times 10^{-3} \text{ cm}^2/\text{Vs}$ under standard conditions (Gu, Wang, Schiff, Li, and Malone, 1994, and references therein).

There have been several indications recently that this apparent limit to the hole drift mobility of a-Si:H based materials may be surmounted. In particular Ganguly and Matsuda (1995) have reported much larger values for the hole mobility in a-Si:H deposited under carefully chosen conditions in a “triode” reactor. This work has not yet been confirmed by other laboratories. Here we first present hole drift mobility measurements in a-Si:H deposited using the “hot-wire” technique. Although there is a significant range of hole mobilities in these specimens, we have measured values as large as $10^{-2} \text{ cm}^2/\text{Vs}$, five times the value for conventional a-Si:H alloys. We also report measurements consistent with earlier work by Ganguly and Matsuda showing high hole mobilities in their materials.

Time-of-Flight Measurements in Hot-Wire Material

Specimens and Instruments

The measurements reported here were obtained on a 2.3 μm hot-wire layer deposited onto stainless steel, forming a Schottky barrier structure. A 40 nm n^+ a-Si:H top layer was plasma-deposited onto the hot-wire layer, and a thin Pd film evaporated onto the n^+ layer. The structure was prepared at the National Renewable Energy Laboratory (NREL). Descriptions of the hot-wire deposition procedures and of additional structural and transport characterizations have been given elsewhere (Mahan and Vanecek, 1991; Crandall, 1992). Here we restrict ourselves to noting that the hot-wire material used in the present study is amorphous (based on Raman measurements), has about 2 atomic % of hydrogen and a “Tauc” bandgap of 1.60 eV. The thickness was measured on a co-deposited substrate using a mechanical profilometer. Although the hole drift mobility varied substantially on a single substrate, the thickness variation across the substrate was negligible. Specimens were studied in their as-deposited state without extensive light exposure.

Time-of-flight measurements were done using a transient photocurrent apparatus; the procedures have been described in detail elsewhere (Wang, Antoniadis, Schiff, and Guha, 1993). We used a pulsed laser tuned to a wavelength of 590 nm, for which we estimate that carrier generation occurred within about 1000 Å of the (top) illuminated Pd/n⁺ interface.

Time-of-flight measurements

In this section we present measurements on the diode which gave the largest hole drift mobility. In Fig. 14 we present normalized photocurrent transients $i(t)d^2/Q_0V$ for several temperatures and a uniform field of $V/d = 69.5$ kV/cm. d is the i-layer thickness, V is the applied voltage, and Q_0 is the photocharge generated in the structure. The normalization eliminates any linear dependence of the photocurrent upon applied bias voltage or laser intensity.

The voltage polarity corresponds to hole transit across the structure. The photocharge Q_0 was estimated by integrating the transient photocurrent $i(t)$. Q_0 varied about 30% with temperature, which we attribute to the temperature-dependent absorption of the n⁺ layer.

The transients have the qualitative form expected for holes in a-Si:H. Consider the lowest curve, corresponding to 200 K. After an initial “peak,” one sees a shallow decay commencing around 2×10^{-7} s. We identify this as the classical, dispersive behavior of the drifting holes prior to the onset of effects due to their sweepout at the opposing electrode. Commencing around 3×10^{-5} s, this transient steepens, which corresponds to the “post-transit” regime of dispersive transport. Similar effects can be discerned for all temperatures, although the present figure makes detailed separation of the current transients for differing temperatures somewhat difficult.

In addition to this well-known dispersive form for the transient photocurrent at longer times, Fig. 14 reveals a relatively temperature-independent peak at the earliest times ($t < 100$ ns). We attribute this to electron transit across the photogeneration region (first 1000 Å in the n-layer side). The time-scale of this signal is determined by the capacitance of the diode in conjunction with the 50 Ohm impedance of the electronics and cables.

Time-of-flight estimates of a drift mobility μ_b are based on the expression:

$$\mu_b = L/E t_T$$

where L is the average displacement of the photocarriers at the transit time t_T , and E is the (uniform) applied electric field. Dispersive photocarrier transport implies that this drift mobility depends strongly upon the ratio L/E .

In order to compare the mobilities from different materials it is essential to specify a particular value for L/E which must be used for all specimens (Wang, *et al*, 1993). To obtain the transit times corresponding to a standard value of L/E , we integrate the normalized photocurrents in Fig. 14; this yields a plot of L/E vs. t , as shown in the lower portion of Fig. 14. The tendency of the charge plots to saturate around 3×10^{-9} cm²/Vs corresponds to sweepout: the maximum displacement of a hole is the sample thickness of 2.3 μm, so for the present plot the maximum value of $L/E = 3.4 \times 10^{-9}$ cm²/Vs.

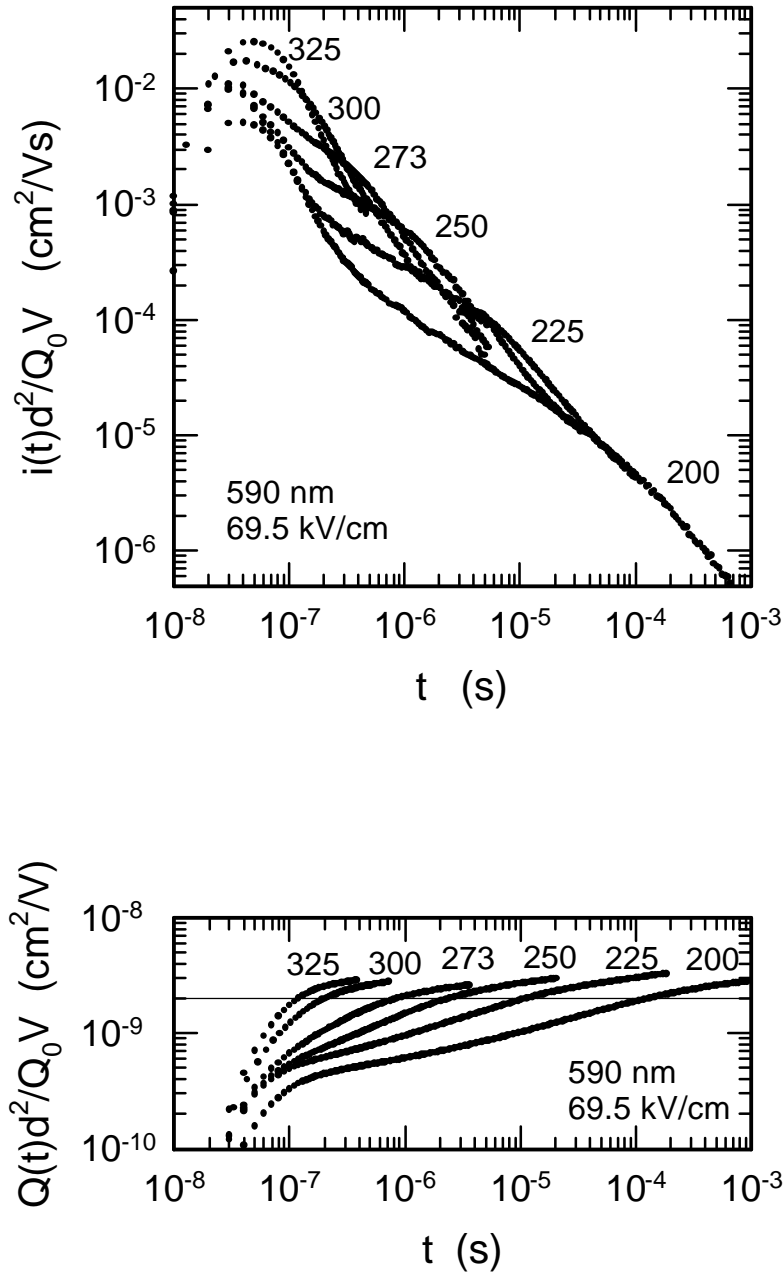


Fig. 14. (upper) Normalized transient photocurrents $i(t)d^2/Q_0V$ for holes measured at $\lambda = 590 \text{ nm}$ at several temperatures and constant electric field of 69.5 kV/cm . (lower) Logarithmic plot of $Q(t)d^2/Q_0V$ for the same conditions as the transients; for times sufficiently early that carriers have not yet been swept completely across the structure, the charge transient measures the time dependence of $L(t)/E$ of the hole displacement $L(t)$ to the electric field E . The intersection of each curve with the line at $2 \times 10^{-9} \text{ cm}^2/\text{V}$ determines the transit times used to calculate a standard drift mobility.

We chose a “standard” value of $L/E = 2 \times 10^{-9} \text{ cm}^2/\text{V}$ for reporting μ_h , which corresponds to transit across a structure of thickness $0.6 \text{ }\mu\text{m}$ at 0.9 V applied bias. $L/E = 2 \times 10^{-9} \text{ cm}^2/\text{V}$ was also used in previous work on electron transport in a-SiC:H and a-SiGe:H by Wang, *et al* (1993a, 1993b) and for hole transport by Gu, *et al* (1994). The horizontal line in the lower portion of Fig. 14 indicates this value for L/E ; the transit times used for computing μ_h are obtained from the intersection of this line with the measured $Q(t)$ curves at various temperatures.

Time-of-Flight Measurements in Triode Materials

Electrotechnical Laboratory in Japan has previously reported remarkably large *hole* drift mobilities in a Si:H materials deposited in a narrow range of conditions in a triode plasma deposition reactor [6]. The materials are deposited directly onto crystalline silicon substrates. Dr. Gautam Ganguly has sent us several samples for us to check whether we can reproduce the Electrotechnical Laboratory measurements. The samples had top metal contacts and form adequate Schottky barrier diodes.

In Fig. 15 below we show some of the transient photocurrent transients we measured which are consistent with hole sweepout. Measurements were done with 505 nm illumination through the top metal contact; under reverse bias holes photogenerated near the a Si:H/metal interface are swept across the diode to the c-Si:B substrate. The transients are normalized by the reverse bias voltage. There is

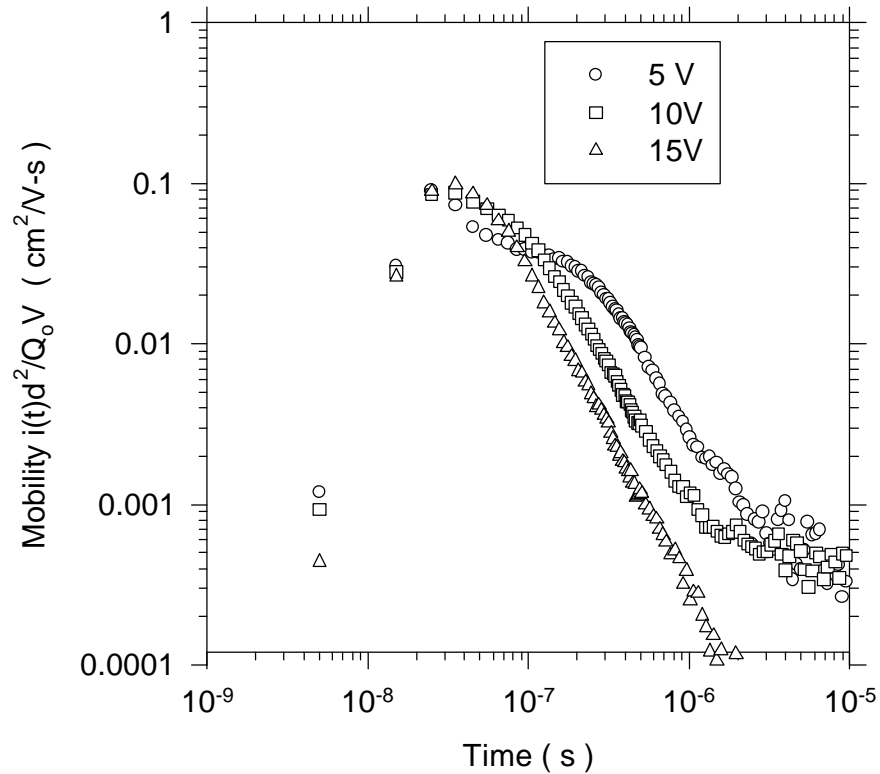


Fig. 15: Normalized transient photocurrents measured at 300 K in a triode-deposited a-Si diode (c-Si:B/a Si:H/m) prepared at Electrotechnical Laboratory (505 nm illumination through the metal layer). Results are shown for 3 reverse-bias voltages. The total photocharge Q_0 was measured by integrating the 15 V transient. The transients show the characteristic features expected for sweepout of holes.

some non-Ohmicity for shorter times which we have not explained. Nonetheless the general features of time-of-flight measurements are clearly seen. For example, the 5 V transient shows a reasonably clear downturn or “kink” at about 300 ns. The position of this kink clearly at shorter times for larger voltages. The vertical axis can be interpreted as a “transient mobility.”

Results

In Fig. 16 we have plotted the measured hole drift mobilities μ for the best hot-wire specimen semilogarithmically against reciprocal temperature $1/T$; we show results at two values of L/E . We also show previously published hole drift mobility measurements from our laboratory (Gu, *et al*, 1994) on a “standard” a-Si:H sample prepared at Energy Conversion Devices, Inc. using a diode-type plasma deposition reactor. These measurements on “standard” a-Si:H are consistent with completely independent work from at least two other laboratories. The hole mobilities measured for the HW a-Si:H specimen are significantly higher than the measurements on conventional a-Si:H.

The solid lines in Fig. 16 are our fits to the measurements using the exponential bandtail multiple-trapping model for the hole drift mobility:

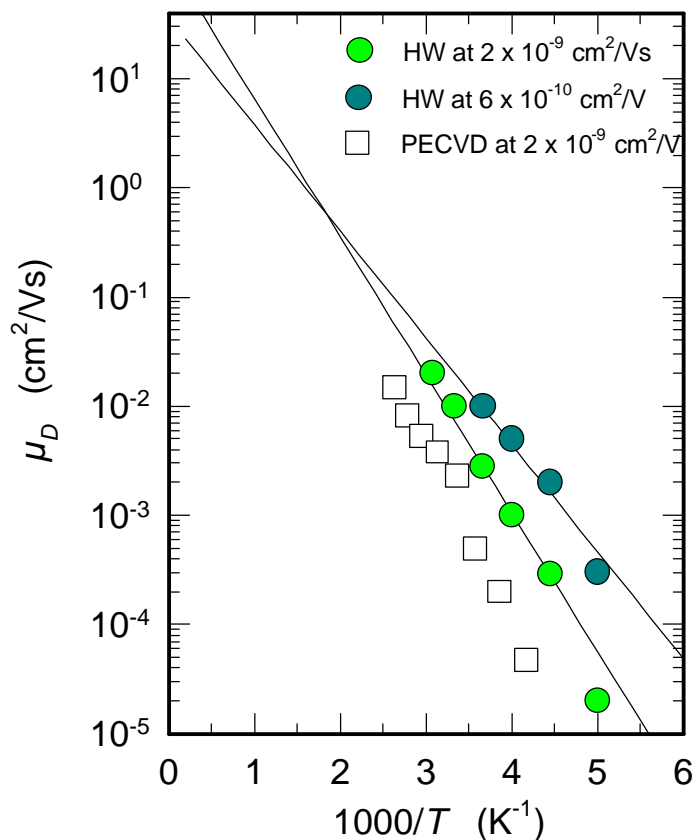


Fig. 16. Semilogarithmic plot of average hole drift mobility μ as a function of reciprocal temperature $1000/T$ for indicated values of displacement/field ratio L/E . Results are shown for a hot-wire (HW) sample and a conventional plasma-deposited (PECVD) sample of a-Si:H.

$$m_D = m_0 \left(\frac{Ln}{m_0 E} \right) \left[\frac{Ln}{m_0 E} \right]^{-E_0/kT} \quad (13)$$

where E_0 is the characteristic energy of the exponential valence bandtail, μ_0 is the “microscopic” mobility of holes, and v is an “attempt-to-escape” frequency for holes trapped in the valence bandtail. The multiple-trapping model gives an acceptable fit. Unfortunately, no single parameter accounts for the increase in the hole mobility in the hot-wire material. Additional measurements at higher temperatures and for a larger range of L/E values would probably clarify this issue, but we were unable to execute such measurements in the present specimens.

In Fig. 17 we present a similar plot showing hole mobility measurements for two triode-deposited samples and for conventional a-Si:H. The triode samples correspond to the upper regression curves, and have mobilities near room temperature nearly 100 times higher than for conventional a-Si:H. The open symbols are previously reported hole mobilities from Ganguly, *et al*, (1996) which are consistent with the present measurements.

We have plotted the correlation of hole drift mobility measurements with the optical bandgap for a variety of specimens at room-temperature under the standard condition $L/E=2 \times 10^{-9} \text{ cm}^2/\text{Vs}$. The cluster

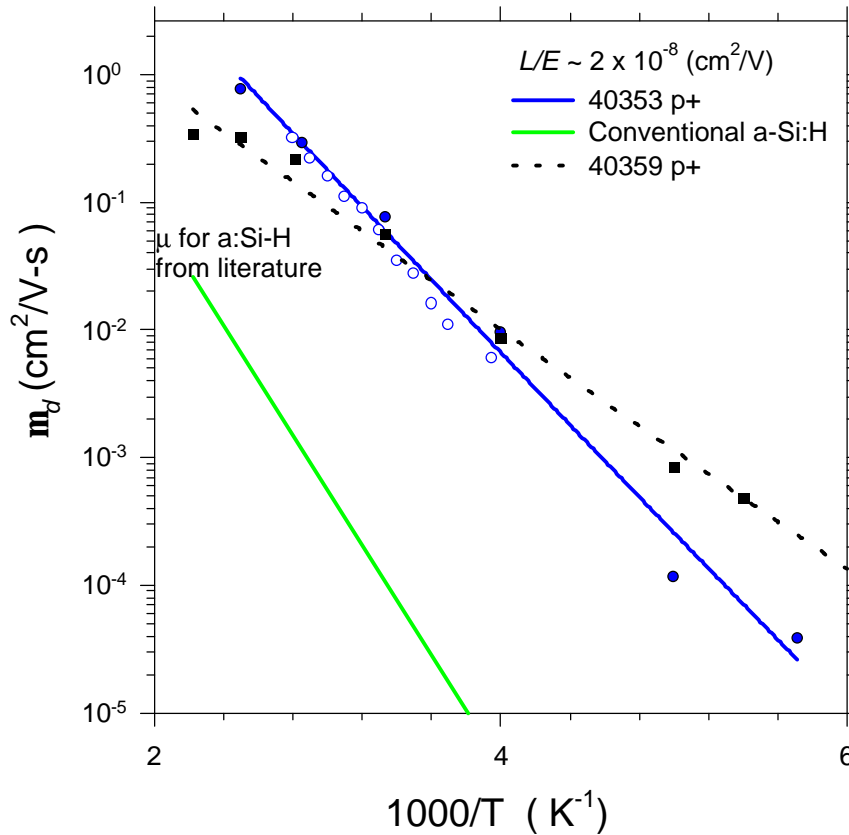


Fig. 17: Hole drift mobility for conventional plasma-deposited a Si:H (Gu, *et al*, 1994) and for “triode” plasma deposited a Si:H from Electrotechnical Laboratory. The upper two regression lines represent the triode-material; the open symbols represent prior measurements of Ganguly, *et al* (1996).

of solid symbols at 1.6 eV represents numerous measurements on hot-wire a-Si:H; we have found considerable variability in our measurements. We believe this represents an underlying variability in the hot-wire materials since we have generally obtained much narrower variance for standard a-Si:H. On the figure we have also indicated using an arrow the very large hole mobilities measured by Ganguly, *et al* (1996) in triode-deposited a-Si:H, and confirmed in Fig. 17; it is probably worth noting that these authors also report considerable variability in their hole measurements.

We comment briefly on whether the relatively large hole mobilities we have measured could have been inferred from earlier measurements of large hole diffusion lengths in similar materials. We note that neither parameter can be predicted from the other. In the following section we show that diffusion length measurements in “standard” a-Si:H can be predicted from knowledge of *both* the hole drift mobility (as a function of L/E) and the recombination response time. It is likely that improved hole drift mobilities may play a role in the improved diffusion length, but a complete understanding of the latter requires an understanding of electron-hole recombination as well as of hole transport.

Relationship of Ambipolar Diffusion Length Measurements and Hole Drift Mobilities in a-Si:H

The ambipolar diffusion-length L_{amb} is one of the measured properties of an a-Si based material used to infer photovoltaic quality. The interpretation of this parameter is well-known to semiconductor device scientists; roughly, the parameter indicates how far the *less mobile* carrier in a semiconductor diffuses before it recombines with the more mobile carrier.

The strong interest in L_{amb} in recent years has occurred because of the development of a simple experimental technique for measuring it. This is the *steady state photocarrier grating* measurement developed by Ritter, Zeldov, and Weiser (1986). It has been used for this purpose in the development of

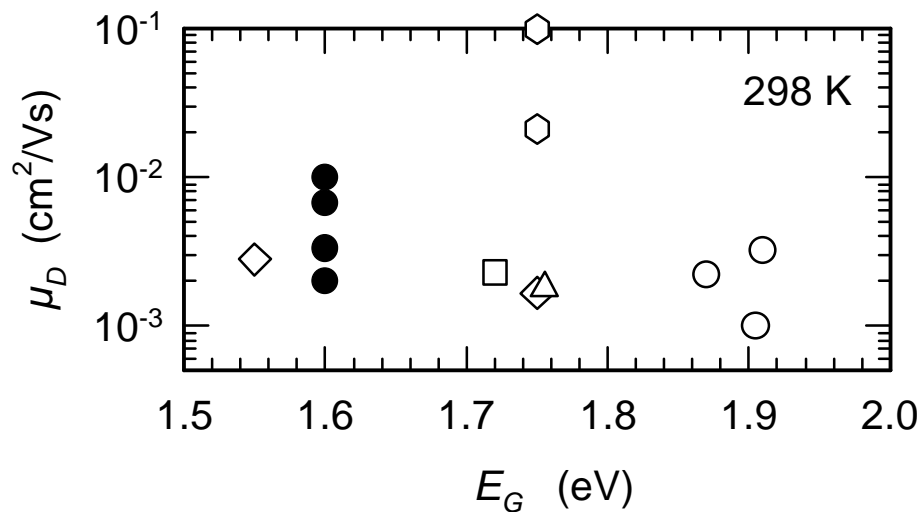


Fig. 18. Summary of hole drift mobility measurements at 298 K evaluated at $L/E = 2 \times 10^{-9} \text{ cm}^2/\text{V}$ as a function of bandgap. Solid circles: present measurements on hot-wire material from NREL. Diamonds - a-SiGe:H alloys (Nebel, *et al*, 1989). Circles - a-SiC:H alloys (Gu, *et al*, 1995). Hexagon - “triode” a-Si:H (Ganguly, *et al*, 1996). Square - a-Si:H (Gu, *et al*, 1996). Triangle - a-Si:H (Tiedje, *et al*, 1984).

hot-wire a-Si:H at NREL, of a-SiC:H at Solarex, and elsewhere. Despite this popularity, there is little understanding of the meaning of L_{amb} , so its success as a photovoltaic materials quality factor is based on phenomenological correlations.

The importance of our work for photovoltaic properties is the following. There are several plausible recombination channels for holes in a-Si:H which are, for example, all incorporated into standard device models such as AMPS. The advance we have made is that we can subject each channel to a very severe, quantitative constraint: the ambipolar diffusion length must agree numerically with estimates of the hole drift mobility and the Einstein relation $D = (kT/q)\mu$ of diffusion constant and mobility.

The particular model for which we obtain agreement is illustrated in Fig. 19. The curve labeled “drift” is compatible with hole time-of-flight measurements in a-Si:H (Tiedje, 1984; Gu, *et al*, 1994b). It shows the function $x(t)$ indicating how far a hole drifts under the influence of an electric field as a function of time; the particular form for $x(t)$ is apparently dictated by multiple-trapping in the valence bandtail (Tiedje, 1984).

The curve labeled “diffusion and recombination” is a reasonable model for the mean-square diffusion $(\delta x)^2$ of a hole as a function of time: Given the Einstein relation, the normalized hole diffusion should agree with the time-of-flight measurement at short times (the bandtail multiple-trapping regime). At longer times, after an electron annihilates the hole near a recombination response time τ_R , the diffusion approaches the diffusion length L_D . Note that this view neglects the “deep-trapping” by a dangling bond prior to recombination.

In Fig. 20 we show the correlation of the measured average diffusion constant D with the average mobility μ . These results were obtained on several intrinsic a-Si:H materials prepared by plasma-deposition at the Technical University of Munich and at Syracuse University.

The average diffusion constant is obtained from SSPG and photoconductivity response time measurements on thin films deposited onto glass with coplanar metal contacts (see Wang and Schwarz,

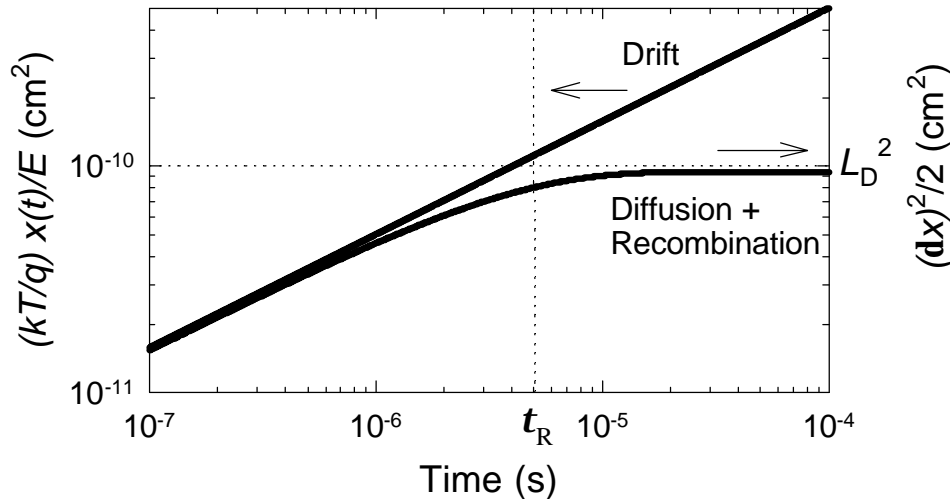


Fig. 19: Proposed model for the relationship of hole drift and diffusion measurements. Drift measurements are made under recombination free conditions; diffusion measurements usually yield only the diffusion length L_D , which is determined by the hole diffusion truncated at the recombination time τ_R .

1994 for details; the actual measurements are presented in Gu, Schiff, Grebner, Wang, and Schwarz, 1996). In particular we evaluate as $D_h = L_{amb}^2 / 2\tau_R$, where L_{amb} is the ambipolar diffusion length actually measured by SSPG and τ_R is the recombination response time measured from the photoconductivity decay time. Note that D_h depends upon the illumination intensity used for the measurements.

The average mobility is based on the function $x(t)/E$ measured in time-of-flight for holes; these measurements are conducted under near-dark conditions, and are reported in Gu, *et al* (1996). The mobility is then calculated using $x(t)/E$ as evaluated at the same response times used to calculate D_h : $\mu_h = x(t_R)/Et_R$. The TOF measurements were done on Schottky barrier structures; the a-Si:H films were co-deposited with the coplanar electrode samples used for SSPG. Remarkably, the completely different experiments yield results which are consistent with the Einstein relation over some three orders of magnitude. We believe that the remaining discrepancy is due to some approximations in the standard analysis of the ambipolar diffusion length measurement (Ritter, Zeldov and Weiser, 1988; Wang and Schwarz, 1994). A discussion of the more general theoretical situation is given in the published article presenting this work (Gu, Schiff, Grebner, Wang, and Schwarz, 1996). An analysis which may improve on that presented here, and which reduces the deviation between the experimental data and the Einstein relation, has been proposed by Brueggemann (1997).

One other interesting fact -- other than the probable validity of the Einstein relation -- can be deduced from these results. Hole deep-trapping has been measured using time-of-flight techniques (see Liu, Maruyama, Wagner, and Delahoy, 1989, for some measurements); this process most likely corresponds to the capture of a hole by a dangling bond at sufficiently long times. Since time-of-flight is done under near dark conditions, it is unclear whether a hole is also "deep-trapped" prior to its recombination under

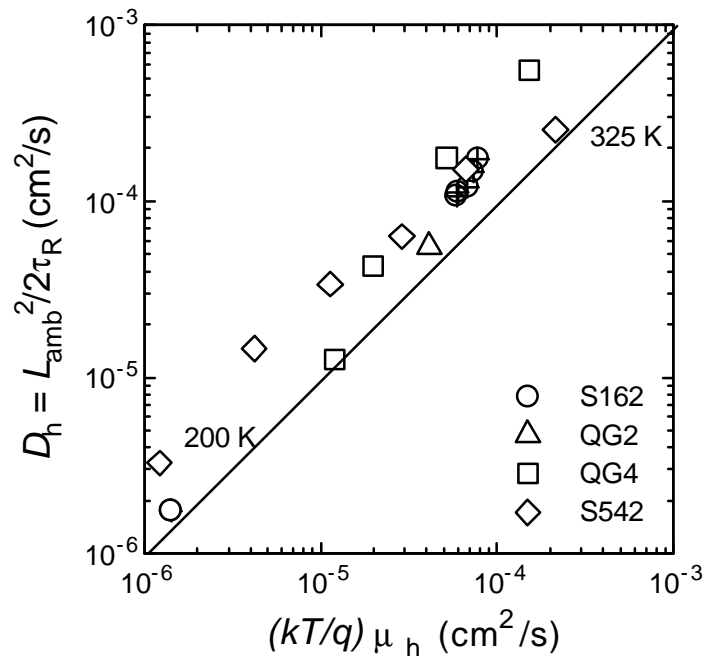


Fig. 20. Correlation of the hole diffusion coefficient D_h with the "Einstein normalized" hole drift mobility $(kT/q)\mu_h$; both are averaged from their photogeneration up to recombination at time τ_R . Measurements for four specimens over a range of temperatures and illumination intensities are indicated. The Einstein relation $D_h = (kT/q)\mu_h$ is indicated by the solid line.

normal solar illumination conditions. The results we have just presented show that ambipolar diffusion under solar illumination conditions is complete at times prior to hole deep trapping; in other words, annihilation of holes by electrons occurs before the holes are deep-trapped in a-Si:H under reasonable illumination intensities.

Photocapacitance and Hole Drift Mobility Measurements in Hydrogenated Amorphous Silicon

Introduction

The spatial profile of the space-charge inside semiconductor diodes is an elementary, textbook calculation for crystalline silicon (c-Si) and other well-understood semiconductors. Capacitance measurements offer convincing proof of the validity of these calculations in ideal cases. For highly insulating and photoconductive semiconductors such as hydrogenated amorphous silicon (a-Si:H) an equally significant issue is the profile of photocharge inside the device; photocharge is created by illumination, and is central to applications as solar cells or light sensors. Photocapacitance is then perhaps the most direct measurement addressing the photocharge profile (Crandall, 1983).

Previous work by Wang and Crandall (1996) using a combination of photocapacitance measurements, solar cell parameter measurements, and computer modeling has shown that photocharge buildup inside solar cells causes field collapse and degradation of the conversion efficiency for higher illumination intensities. In the present paper we seek a deeper understanding of the origin of these effects. We present photocapacitance measurements in an a-Si:H Schottky barrier diode which appear quite consistent with those of Wang, *et al* (1996). We show that these measurements can be understood relatively simply using the dispersive drift-mobilities of holes measured over the last twenty years. Dispersion is the phenomenon that drift-mobilities decline rapidly as the distance across which they are measured increases. This successful fitting clarifies the role of low hole mobilities in space-charge formation of a-Si:H solar cells under illumination, and shows that photocapacitance can be used essentially as an impoverished scientist's technique for measuring dispersive hole drift mobilities.

Samples and Photocapacitance measurements

We measured the photocapacitance in one plate of a-Si:H Pd Schottky diodes prepared at Pennsylvania State University. The structure was deposited on a glass substrate in the sequence $m/n^+/i/Pd$, where m indicates a semitransparent metal back contact, n^+ indicates heavily phosphorus-doped a-Si:H layer plasma-deposited from silane/phosphine mixtures, i indicates an undoped, plasma-deposited a-Si:H layer, and Pd indicates a semitransparent top metal electrode. The latter forms a Schottky barrier with the intrinsic layer; similar structures have been used extensively for internal photoemission measurements in earlier work (Chen and Wronski, 1995). We have measured the built-in potential on this device using the electroabsorption method (Jiang, et al, 1996); we obtained $V_{bi} \approx 0.4$ V.

Capacitance measurements were performed using a sinusoidal wave generator and lockin amplifier detection of the amplitude and phase of the resulting currents flowing into the device. Low-intensity, linear photocapacitance measurements were done using chopped monochromator illumination and a second lockin to detect the modulation of the signal from the first, capacitance-detecting lockin. In turn these lockin signals were used as inputs for computer-based signal averaging of sweeps either of the DC, reverse bias potential or of the monochromator wavelength.

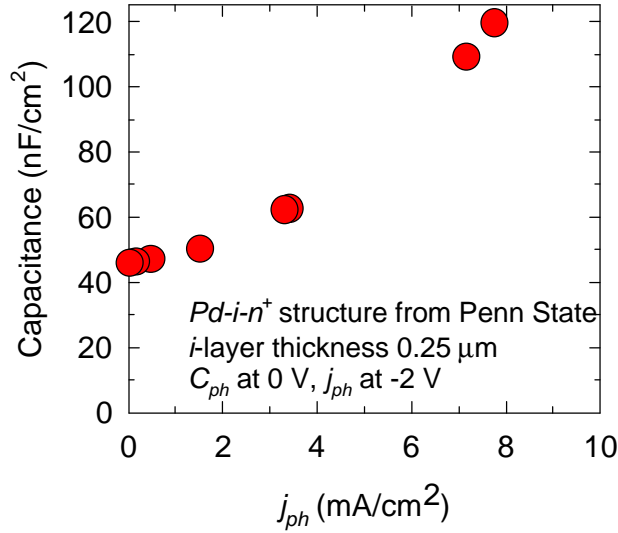


Fig. 21: Short-circuit capacitance measurements as a function of photocurrent (at -2 V) in a Schottky diode specimen. Illumination was at 633 nm.

By way of introduction, in Fig. 21 we illustrate the capacitance measured under short-circuit conditions as a function of illumination intensity using a helium-neon laser (633 nm wavelength). We used the photocurrent measured at -2 V bias as a proxy for illumination intensity. For small illumination intensities (and photocurrents) the capacitance has essentially its dark value; we used this value to estimate the thickness of the sample for later use in modeling. It is clear that for photocurrent densities exceeding about 1 mA/cm² the capacitance starts to rise discernibly;

The onset of discernible photocapacitance in Fig. 21 is an indication that the net space charge stored in the insulating, intrinsic layer of the Schottky diode has become comparable to the charge $CV_{bi} \approx 20$ nF/cm². One objective of the present research is to understand the magnitude of this photocurrent threshold.

We approach this problem by measuring the *linear photocapacitance* for illumination intensities so low as to negligibly disturb the dark electric field profile inside the Schottky diode. We define the linear photocapacitance as:

$$C'_p \equiv C_p / i_p, \quad (14)$$

where i_p is the DC photocurrent flowing through the device and C_p is the photocapacitance measured at some specified reverse bias potential.

In practice, the illumination intensity from our monochromatic illuminator satisfied this low-intensity requirement. We present some of these voltage-dependent measurements as Fig. 22 using 600 nm illumination, which is nearly uniformly absorbed in within the Schottky diode. The DC photocurrent shows a modest increase with reverse bias voltage. The effect presumably corresponds to a reduction in electron-hole recombination, since the volume charges of both carriers is reduced by the reverse bias. Nonetheless this dependence does surprise us somewhat, since we expected recombination effects to be negligible for such low intensities.

The linear photocapacitance shows a rapid decline – essentially to zero -- as the reverse bias increases. The effect can be understood qualitatively from the decrease in photocarrier transit times under reverse

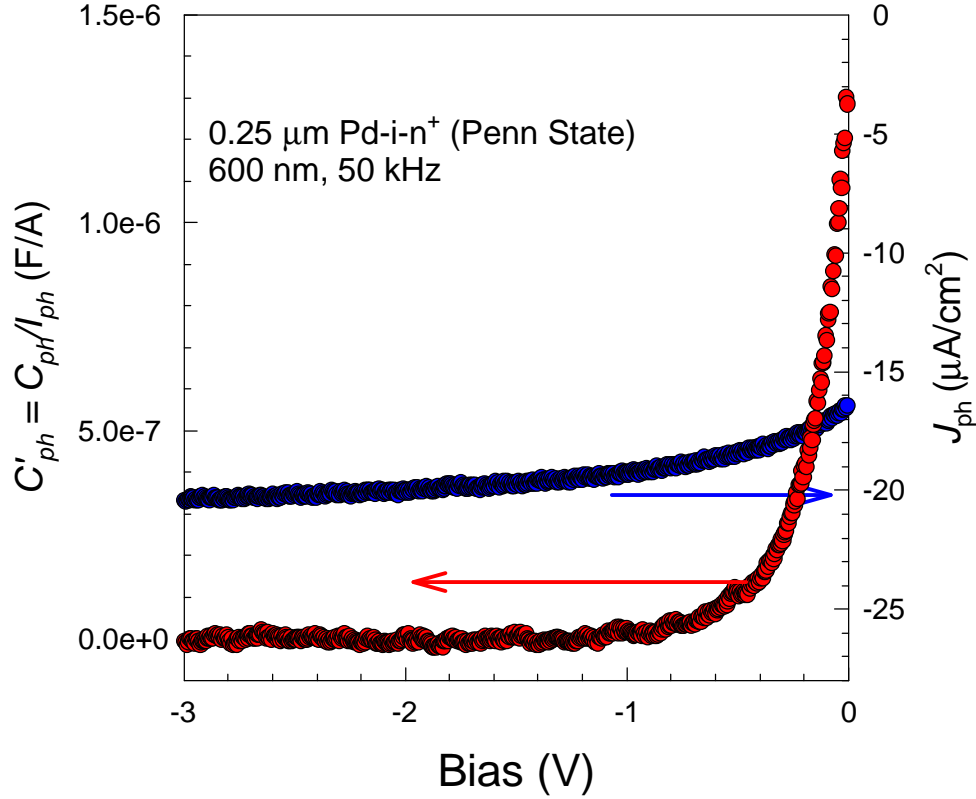


Fig. 22: DC photocurrent density J_{ph} and linear photocapacitance $C'_p(V)$ as a function of potential across the Schottky diode specimen.

bias; as transit times are diminished, so too is the stored photocharge which is monitored by the capacitance measurement.

We also conducted extensive measurements of the wavelength-dependence of the photocapacitance using illumination both through the back Pd top electrode and through the n^+ bottom electrode. We used this approach to move the position where photogeneration occurs throughout the intrinsic layer of the diode. The measurements, which will not be presented here, are consistent with the conclusion that holes determine the linear photocapacitance at low intensities. In essence we find that, as the photogeneration of holes occurs closer to the collecting, Pd electrode, the photocapacitance diminishes monotonically. The conclusion is consistent with the observation that, for a-Si:H, electrons are far more mobile than holes, and are consequently swept out of the structure much more rapidly than holes.

Model for photocapacitance and dispersive transport

We first recast the theory for photocapacitance due to a single carrier obeying the normal, “non-dispersive” form for transport. This recasting involves using the definition of the carrier mobility in a slightly unconventional way, in which carrier drift $x(t)$ in an electric field E following photogeneration at $t = 0$ is written:

$$x(t)/E = m_0 t \quad . \quad (15)$$

We assume steady-state photogeneration in a thin sheet near the n⁺/i interface and a uniform field $E = V/d$ across the intrinsic layer of thickness d . The field drifts the holes across the specimens; electrons are swept into the electrode layer instantaneously. The resulting photocurrent density is denoted j_p . Since the holes spend some transit time t_T traversing the sample, they are associated with a positive space-charge density \mathbf{r} . We use an apparently inconvenient definition for the transit time: t_T is the time required for the holes to drift halfway (ie. $d/2$) across the sample. Then we have:

$$t_T = \frac{d}{2m_0 E} = \frac{d^2}{2m_0 V} \quad (16)$$

For uniform illumination, this expression should be halved – reflecting the fact that the holes need travel only half as far (on average) to reach the collecting electrode.

The space-charge density, which is spatially uniform for this model, is then given by:

$$\mathbf{r} = \frac{2j_p t_T}{d} \quad (17)$$

An external photocharge density \mathbf{s}_p flows to the electrodes to maintain a constant potential. This density is slightly different than the integrated space-charge of the holes inside the sample, since it reflects the uniform spatial distribution of the holes; one obtains:

$$\mathbf{s}_p = \mathbf{r}d / 2 \quad (18)$$

Capacitance measurements involve measuring the current response \mathbf{di}_{90} in quadrature to a sinusoidal voltage modulation. By definition, $C \equiv \mathbf{di}_{90}/\mathbf{w}dV$, where \mathbf{w} and dV are the modulation frequency and amplitude, respectively. As might be anticipated, the photocapacitance per unit area C_p (that is, the change in capacitance due to illumination) is related to derivative of this photocharge density with respect to the external voltage:

$$C_p \equiv -\frac{\mathbf{I}\mathbf{s}_p}{\mathbf{I}V} = -(d/2) \frac{\mathbf{I}\mathbf{r}}{\mathbf{I}V} \quad (19)$$

Despite the simplicity of this expression, we have found no trivial explanation for its negative sign. It emerges from a fairly tedious treatment of fields, space charges, and displacement currents which we do not reproduce here. Note, however, that the quadrature current must be considered in conjunction with a dissipative current modulation \mathbf{di}_0 . In any event, the photocapacitance expression can be rewritten very usefully as follows:

$$C_p = -j_p \frac{\mathbf{I}t_T}{\mathbf{I}V} \quad (20)$$

which for the case of non-dispersive transport yields

$$C'_p \equiv C_p / j_p = \frac{d^2}{2m_0 V^2} \quad (21)$$

This expression agrees (to within the factor of 2) with that used by Wang, *et al* (1996).

We now simply extend the application of this expression to the case of dispersive transport. For holes in a-Si:H we used the following expression for the dispersive drift $x(t)$ of holes at room temperature and in a uniform field E :

$$x(t) / E = (m_0 / n)(nt)^a \quad (22)$$

The sublinear increase of $x(t)$ with time is the phenomenon of dispersion; it causes drift mobilities to depend upon the length-scale or the time-scale upon which they are measured. The parameters m_0 , n ,

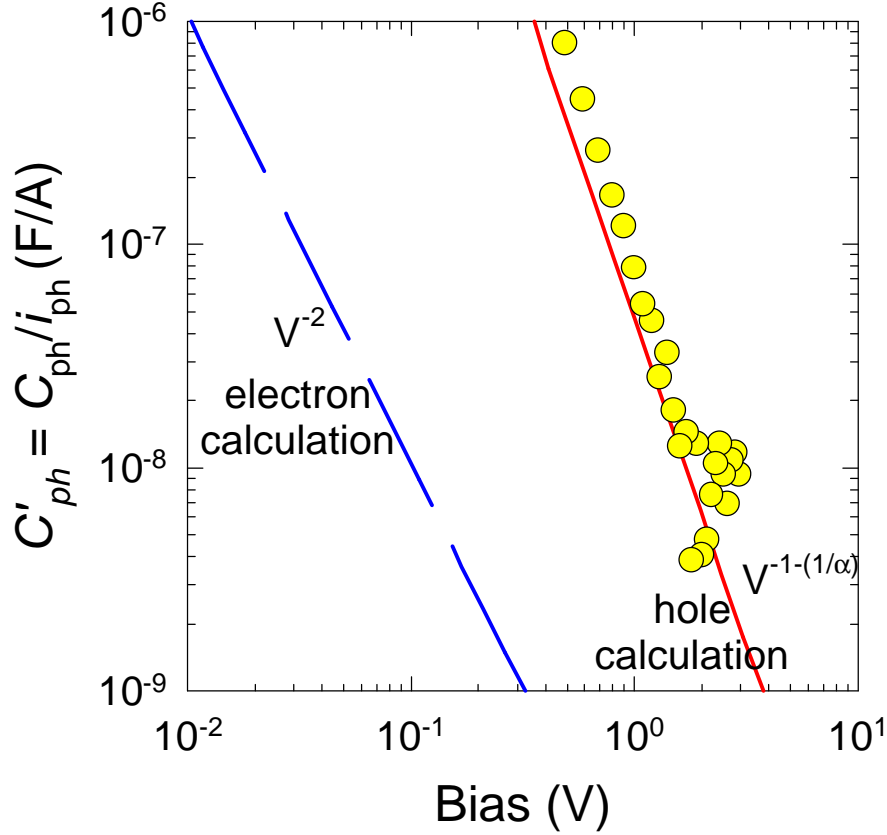


Fig. 23: Comparison of calculations of linear photocapacitance with measurements in an a-Si:H Schottky barrier diode. The electron and hole calculations are based on time-of-flight mobility measurements and their corresponding non-dispersive and dispersive theories. The measurements were at 650 nm; the voltage bias axis for the measurements has been shifted by 0.4 V to account for the built-in potential of the diode.

and \mathbf{a} are determined by measurement; we shall use the relatively recent paper of Gu, *et al* (1994), who also review most earlier work on holes in a-Si:H and related alloys. Eq. (22) may be derived from bandtail multiple trapping, which predicts (in agreement with experiment) that $\mathbf{a} = kT/\mathbf{e}_0$, where \mathbf{e}_0 is the characteristic energy for an exponential bandtail. The transit-time is obtained by substituting $d/2$ for $x(t_T)$, and solving for t_T :

$$t_T = \mathbf{n}^{-1} \left[d^2 \mathbf{n} / 2V\mathbf{m}_0 \right]^{1/\mathbf{a}} \quad (23)$$

We obtain the linear photocapacitance in the form:

$$C'_p \equiv C_p / j_p = (1/\mathbf{a}nd) \left[d^2 \mathbf{n} / 2\mathbf{m}_0 \right]^{1/\mathbf{a}} V^{-1/\mathbf{a}-1} . \quad (24)$$

Again, this expression can be adapted for uniform photogeneration by halving the expression inside the square brackets.

Comparison of photocapacitance and drift-mobility measurement

In Fig. 23 we have plotted the linear photocapacitance $C'_p(V)$ predicted for electrons in a-Si:H as the dashed line. We used a conventional value $\mu_0 = 1 \text{ cm}^2/\text{Vs}$ for the electron mobility. The result for non-dispersive transport (eq. (21)) was halved to account for uniform illumination. Similar, we plot our prediction for $C'_p(V)$ for holes as the solid line. We used the parameters of for intrinsic a-Si:H suggested by Gu, *et al* (1994) ($\nu = 7.7 \times 10^{10} \text{ s}^{-1}$, $\mu_0 = 0.27 \text{ cm}^2/\text{Vs}$, $\mathbf{a} = kT/\mathbf{e}_0$, with $\epsilon_0 = 48 \text{ meV}$); at room-temperature $1/\alpha = 1.92$. Again, we modified the dispersive transport prediction eq. (25) to account for the use of uniform illumination. Finally we plot our measurements of $C'_p(V)$ at 650 nm as the symbols in this figure; the bias voltage is corrected for the built-in potential by assuming $V = V_{\text{external}} - V_{\text{bi}}$, with $V_{\text{bi}} = 0.4 \text{ V}$. The agreement of the model predictions using hole mobilities with the photocapacitance measurements seems very satisfactory to us; we emphasize that we made no adjustments to the hole parameters to gain this agreement.

Appendix

$$E_0(t) = (V/d)(1 + \mathbf{a} \exp(-i\mathbf{w}t))$$

$$\mathbf{r}(t) = \mathbf{r}_0 \{1 - \mathbf{a}_1 \exp(-(kx - \mathbf{w}t))\}$$

$$\mathbf{r}_0 \equiv j_G / v_D (V/d)$$

$$k \equiv \mathbf{w} / v_D$$

$$\mathbf{a}_1 = \mathbf{a} \left\{ \frac{\mathbf{v}_D}{\mathbf{E}} \right\}$$

$$E_1(t) = (\mathbf{r}_0 / \mathbf{e}_0) \left[(x - d/2) - (\mathbf{a}_1 / ik) \exp(-i\mathbf{v}t) \left\{ \exp(ikx) - \frac{(\exp(ikd) - 1)}{ikd} \right\} \right]$$

$$j_{1d} \approx \mathbf{a}_1 \mathbf{r}_0 (\mathbf{v} / k) \exp(-i\mathbf{v}t) \{ \exp(ikx) - 1 - ikd/2 \}$$

$$j_{1d} = \mathbf{a}_1 j_G \exp(-i\mathbf{v}t) \{ -ikd/2 - 1 + \exp(ikx) \}$$

$$C_p = (-ikd/2)(\mathbf{a}_1 j_G) / (-i\mathbf{v} \mathbf{a} V)$$

$$C_p = (\mathbf{a}_1 j_G) / (2\mathbf{a} E v_D)$$

$$C_p = (j_G / 2v_D^2) \frac{\mathbf{v}_D}{\mathbf{E}}$$

$$C_p = -(j_G) \frac{\mathbf{t}_T}{\mathbf{V}}$$

$$t_T = d / 2v_D$$

Search for Novel p^+ materials

One component of this project has been a search for novel p^+ materials to act as the window layer for a triple-junction solar cell. The rationale for this research is the argument that the open circuit voltage for wide bandgap cells ($E_T > 1.9$ eV) is limited by the properties of the window layers presently in use (amorphous SiC:H, and microcrystalline Si). For the middle and narrow bandgap cells it is generally accepted that V_{OC} is limited by the properties of the intrinsic layer of *pin* cell.

In the first year of the project we commenced exploring the properties of boron phosphide films. This choice was based on the fact that crystalline BP has been used as a window layer on crystalline Si solar cells (Takenaka, Takigawa, and Shohno, 1978), and that crystalline BP is a fairly wide bandgap material which should have better optical properties than, for example, microcrystalline Si. Our films were deposited using phosphine (PH_3) as the phosphorus precursor, diborane (B_2H_6) or trimethylboron ($B(CH_3)_3$; typically referred to as TMB) as the boron precursors, and hydrogen. Use of TMB as the precursor of course leads to ternary, boron phosphide/carbide films. All the films were prepared using a commercial RF plasma deposition system operating at 13.56 Mhz.

We describe our work in some detail below. There are two principal results:

- We discovered a conducting, transparent film in a remote area of the reactor. We have not produced comparable films in the standard, interelectrode region of the reactor.
- We have prepared amorphous a-BP:H alloys with good optical properties. We have not yet achieved electrical properties in these films which are satisfactory for application as window layers.

The results from about one dozen depositions are presented as Table 3. The optical absorption

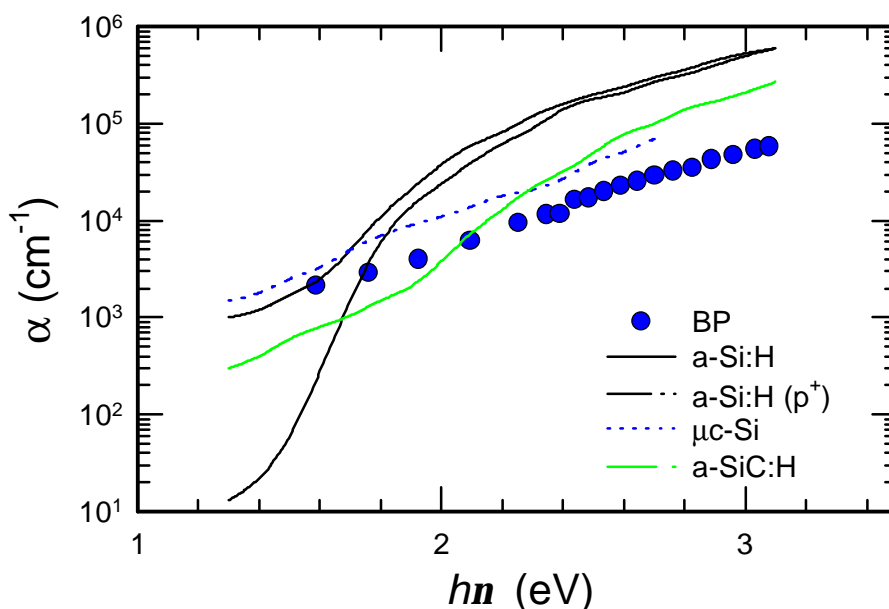


Fig: 24: Comparison of the optical absorption properties of a thin boron-phosphide film (unknown stoichiometry) with literature values for several thin-film silicon materials.

coefficient measured on one specimen is presented (together with the absorption coefficients for several p^+ materials currents used in a-Si:H based cells) in Fig: 24.

In general the films deposited in the interelectrode area were highly insulating. This insulating behavior is probably an indication that the films have an amorphous structure, and a corresponding tendency to have Fermi energies near the middle of their forbidden gap. We confirmed this speculation by X-ray measurements on one film (noted in Table 3).

The sequence of depositions in Table I was designed to search for deposition conditions to yield microcrystalline BP films. We noted in our initial work that no films formed on the platen under relatively high pressure, high power conditions using TMB and PH_3 diluted in H_2 as precursor gases. Since a thin, conducting film was deposited in a remote area of the reactor (ie. not between the two large

Seq. (Date)	T_{sub} ($^{\circ}\text{C}$)	Gas Pressure (mTorr)	Power (W)	$t_{\text{dep.}}$ (min)	Thickness (nm)	σ ($\Omega\cdot\text{cm}$) ⁻¹	n	$E_{\text{act.}}$ (eV)	Comments
111/4/94	water	TMB/ H_2 (2%): 310 PH_3 / H_2 (1%): 860	37.4	121	< 100 nm	$> 8.2 \times 10^{-6}$ at 300 K		0.24	Film deposited only in remote area
21/11/95	250	PH_3 /He(3%): 132 B_2H_6 /He(3%): 70	3.3	98	200	$< 10^{-12}$ at 300 K	3.4		
32/1/95	250	PH_3 /He(3%): 213 B_2H_6 /He(3%): 100 SiH_4 : 4	3.3	110		Very low			Si doping
42/10/95	250	PH_3 /He(3%): 163 B_2H_6 /He(3%): 87 H_2 (100%): 70	3.4	512	1000	9.4×10^{-10} at 404 K	3.4	0.23	H diluted; X-ray shows amorphous structure; Optical measurement shows no clear bandgap.
52/21/95	250	PH_3 /He(3%): 228 TMB/ H_2 (2%): 107	3.7	351	280 (0.133A/s)	Very low	4.2		
63/16/95	250	PH_3 /He(3%): 100 B_2H_6 /He(3%): 50 H_2 (100%): 320	4	300		Very low			
76/21/95	250	PH_3 / H_2 (1%): 255 TMB/ H_2 (5%): 50	5	328		Very low			No film found in remote area
86/27/95	250	PH_3 / H_2 (1%): 320 B_2H_6 / H_2 (5%): 33	6.3	290		Very low			Film peeled after 12-hour exposure to air
97/3/95	250	PH_3 / H_2 (1%): 320 B_2H_6 / H_2 (5%): 30	6.5	210	330 estimated using n=3.4	8×10^{-10} at 300 K			Film peeled after 12-hour exposure to air; is measured in an <i>MiM</i> structure
107/14/95	250	PH_3 / H_2 (1%): 490 TMB/ H_2 (5%): 100	19.6	140		Very low			
117/17/95	water	PH_3 / H_2 (1%): 940 TMB/ H_2 (5%): 180	39	132		4×10^{-5} at 300 K			Film deposited only in remote area.
127/19/95	300	PH_3 / H_2 (1%): 620 TMB/ H_2 (5%): 130	30.5	151		Very low			Film deposited only in the center area.

plates serving as RF electrodes), we attributed the absence of growth to etching by atomic hydrogen in the discharge. Based on an analogy with growth of microcrystalline Si films, which requires high hydrogen dilution and high RF power, we adjusted our deposition conditions until growth just barely occurred on the platen. Thus in run no. 12 we obtained deposition only near the center of the platen.

All films deposited in the conventional interelectrode region proved to be highly insulating, even when we achieved very slow deposition.

Questions for Qing: What would happen if there were no hydrogen dilution? What do the percentages mean?

References

- D. F. Blossey, *Phys. Rev.* **B3**, 1382 (1971).
- D. F. Blossey and P. Handler, in *Semiconductors and Semimetals, Vol. 9: Modulation Spectroscopy*, edited by R. K. Willardson and A. C. Beer (Academic, New York, 1972), 257.
- R. Brüggemann, *Phys. Rev. B* **56**, 6408 (1997).
- L. Brus, *J. Phys. Chem.* **98**, 3576 (1994).
- I. H. Campbell, M. D. Jowick, and I. D. Parker, *Appl. Phys. Lett.* **67**, 3171 (1995).
- R. Carius, F. Finger, U. Backhausen, M. Luysberg, P. Hapke, L. Houben, M. Otte, and H. Overhof, *Amorphous and Microcrystalline Silicon Technology-1997*, edited by S. Wagner, M. Hack, E. A. Schiff, R. Schropp, and I. Shimizu (Material Research Society, Pittsburgh 1997) Vol.467, p. 283.
- I. Chen and C. R. Wronski, *J. Non-Cryst. Solids* **190**, 58 (1995)..
- D. Cotter, H. P. Girdlestone, and K. Moulding, *Appl. Phys. Lett.* **58**, 1455 (1991).
- R. S. Crandall, *Appl. Phys. Lett.* **42**, 451 (1983).
- R. S. Crandall, in *Photovoltaic Advanced Research & Development Project : AIP Conference Proceedings No. 268*, edited by R. Noufi (American Institute of Physics, New York, 1992), p. 81.
- M. Cuniot and Y. Marfaing, *Phil. Mag. B* **57**, 291 (1988).
- C. Delerue, M. Lannoo, G. Allan, and E. Martin, *Thin Solid Films* **255**, 27 (1995).
- R.-C. Fang and L. Ley, *Phys. Rev. B* **40**, 3818 (1989).
- P. M. Fauchet, and I. H. Campbell, *Critical Reviews in Solid State and Materials Sciences* **14**, S79 (1988).
- S. J. Fonash, *Solar Cell Device Physics* (Academic, New York, 1981).
- A. Frova, P. Handler, F. A. Germano, and D. E. Aspnes, *Phys. Rev.* **145**, 575 (1966).
- S. Furukawa and T. Miyasato, *Phys. Rev. B* **38**, 5726 (1988).
- G. Ganguly, I. Sakata, and A. Matsuda, *J. Non-Cryst. Solids* **198-200**, 300 (1996).
- G. Ganguly and A. Matsuda, in *Amorphous Silicon Technology-1994*, edited by E. A. Schiff, *et al* (Materials Research Society, Symposium Proceedings Vol. 336, Pittsburgh, 1994), p. 7.
- B. L. Gelmont, B. T. Kolomiets, T. F. Mazets, and S. K. Povlov, *J. Phys. Paris* **42**, C4-919 (1981).
- Qing Gu, Qi Wang, E. A. Schiff, Y. M. Li and C. T. Malone, *J. Appl. Phys.* **76**, 2310 (1994).
- Qing Gu, E. A. Schiff, S. Grebner, F. Wang, and R. Schwarz, *Phys. Rev. Lett.* **76**, 3196 (1996).
- S. Guha, J. Yang, P. Nath, and M. Hack, *Appl. Phys. Lett.* **49**, 218 (1986).

- S. Guha, J. S. Payson, S. C. Agarwal and S. R. Ovshinsky, *J. Non-Cryst. Solids* **97&98**, 1455 (1987).
- P. Hapke, U. Backhausen, R. Carius, F. Finger, S. Ray, *Amorphous Silicon Technology-1996*, edited by M. Hack, E. A. Schiff, S. Wagner, R. Schropp, A. Matsuda (Material Research Society, Pittsburgh 1996) Vol. 420, p.789.
- N. Hata, T. Kamei, H. Okamoto, and A. Matsuda, *Amorphous and Microcrystalline Silicon Technology-1997*, edited by S. Wagner, M. Hack, E. A. Schiff, R. Schropp, and I. Shimizu, **467** 61(Pittsburgh, 1997).
- Mark S. Hybertsen, *Phys. Rev. Lett.* **72**, 1514 (1994).
- L. Jiang and E. A. Schiff, in *Amorphous Silicon Technology-1996*, edited by M. Hack, *et al* (Materials Research Society, Symposium Proceedings Vol. 420, Pittsburgh, 1996), *in press*.
- L. Jiang, Q. Wang, E. A. Schiff, S. Guha, J. Yang, X. Deng, *Appl. Phys. Lett.* **69**, 3063 (1996)
- J. Z. Liu, A. Maruyama, S. Wagner, and A. Delahoy, *J. Non-Cryst. Solids* **114**, 453 (1989).
- A. H. Mahan and M. Vanecek, in *Amorphous Silicon Materials and Solar Cells*, edited by B. L. Stafford (American Institute of Physics, New York, 1991), p. 195.
- U. Mescheder and G. Weiser, *J. Non-Cryst. Solids* **77**, 571 (1985)
- H. Mimura and Y. Hatanaka, *Appl. Phys. Lett.* **50**, 326 (1987).
- S. Nonomura, H. Okamoto, and Y. Hamakawa, *Appl. Phys. A* **32**, 31 (1983).
- A. Nuruddin and J. R. Abelson, *Appl. Phys. Lett.* **71**, 2797 (1997).
- H. Okamoto, K. Hattori, and Y. Hamakawa, *J. Non-Cryst. Solids* **137&138**, 627 (1991) and **164-166**, 893 (1993).
- C. M. Penchina, *Phys. Rev.* **138**, A924 (1965).
- S. Y. Ren and J. D. Dow, *Phys. Rev. B* **45**, 6492 (1992).
- E. H. Rhoderick, *Metal-semiconductor Contacts* (Oxford, New York, 1988).
- D. Ritter, E. Zeldov, and K. Weiser, *Appl. Phys. Lett.* **49**, 791 (1986).
- D. Ritter, E. Zeldov, and K. Weiser, *Phys. Rev. B* **38**, 8296 (1988).
- H. Shen and F. H. Pollak, *Phys. Rev. B* **42**, 7097 (1989).
- K. Shimizu, T. Shiba, T. Tabuchi, and H. Okamoto, *Jpn. J. Phys.* **36**, 29 (1997)
- D. L. Staebler and C. R. Wronski, *Appl. Phys. Lett.* **31** 292 (1977)
- T. Takagahara and K. Takeda, *Phys. Rev. B* **46**, 15578 (1992).
- T. Tiedje, in *Hydrogenated Amorphous Silicocn II*, edited by J. D. Joannopoulos and G. Lucovsky (Springer, New York, 1984), pp. 261-300.
- Y. Tsutsumi, H. Okamoto, K. Hattori, and Y. Hamakawa, *Philos. Mag. B* **69**, 253 (1994)
- R. Vanderhaghen and C. Longeaud, *J. Non-Cryst. Solids* **114**, 540(1989).
- F. Wang and R. Schwarz, *Appl. Phys. Lett.* **65**, 884 (1994).
- Qi Wang, Homer Antoniadis, E. A. Schiff and S. Guha, *Phys. Rev. B*, **47**, 9435 (1993).
- Qi Wang, E. A. Schiff and Y. M. Li, in *Amorphous Silicon Technology-1993*, edited by E. A. Schiff, M. J. Thompson, A. Madan, K. Tanaka and P. G. LeComber, (Materials Research Society, Symposia Proceedings No. 297 Pittsburgh, 1993), p. 803.
- Q. Wang, E. A. Schiff, and S. S. Hegedus, in *Amorphous Silicon Technology-1994*, edited by E. A. Schiff, *et al* (Materials Research Society, Symposium Proceedings Vol. 336, 1994), p. 365.
- Q. Wang, R. S. Crandall, and E. A. Schiff, in *Proceedings of the 21st Photovoltaics Specialists Conference* (IEEE, 1996), 1113.
- G. Weiser, H. Dersh, and P. Thomas, *Phil. Mag. B* **57**, 721 (1988).
- U. Woggon, S. V. Bogdanov, O. Wind, and V. Sperling, *J. Crystal Growth* **138**, 976 (1994).
- M. Zelikson, K. Weiser, A. Chack, and J. Kanicki, *J. Non-Cryst. Solids* **198-200**, 107 (1996)

REPORT DOCUMENTATION PAGE			Form Approved OMB NO. 0704-0188	
Public reporting burden for this collection of information is estimated to average 1 hour per response, including the time for reviewing instructions, searching existing data sources, gathering and maintaining the data needed, and completing and reviewing the collection of information. Send comments regarding this burden estimate or any other aspect of this collection of information, including suggestions for reducing this burden, to Washington Headquarters Services, Directorate for Information Operations and Reports, 1215 Jefferson Davis Highway, Suite 1204, Arlington, VA 22202-4302, and to the Office of Management and Budget, Paperwork Reduction Project (0704-0188), Washington, DC 20503.				
1. AGENCY USE ONLY (Leave blank)		2. REPORT DATE November 1998		3. REPORT TYPE AND DATES COVERED Final Technical Report, 15 May 1994–15 January 1998
4. TITLE AND SUBTITLE Research on High-Bandgap Materials and Amorphous Silicon-Based Solar Cells, Final Technical Report, 15 May 1994–15 January 1998				5. FUNDING NUMBERS C: XAN-4-13318-06 TA: PV905001
6. AUTHOR(S) E.A. Schiff, Q. Gu, L. Jiang, J. Lyou, I. Nurdjaja, and P. Rao				
7. PERFORMING ORGANIZATION NAME(S) AND ADDRESS(ES) Department of Physics Syracuse University Syracuse, NY 13210				8. PERFORMING ORGANIZATION REPORT NUMBER
9. SPONSORING/MONITORING AGENCY NAME(S) AND ADDRESS(ES) National Renewable Energy Laboratory 1617 Cole Blvd. Golden, CO 80401-3393				10. SPONSORING/MONITORING AGENCY REPORT NUMBER SR-520-25922
11. SUPPLEMENTARY NOTES NREL Technical Monitor: B. von Roedern				
12a. DISTRIBUTION/AVAILABILITY STATEMENT National Technical Information Service U.S. Department of Commerce 5285 Port Royal Road Springfield, VA 22161				12b. DISTRIBUTION CODE
13. ABSTRACT (<i>Maximum 200 words</i>) This report describes work performed by Syracuse University under this subcontract. Researchers developed a technique based on electroabsorption measurements for obtaining quantitative estimates of the built-in potential V_{bi} in a-Si:H-based heterostructure solar cells incorporating microcrystalline or a-SiC:H p layers. Using this new electroabsorption technique, researchers confirmed previous estimates of $V_{bi} \approx 1.0$ V in a-Si:H solar cells with “conventional” intrinsic layers and either microcrystalline or a-SiC:H p layers. Researchers also explored the recent claim that light-soaking of a-Si:H substantially changes the polarized electroabsorption associated with interband optical transitions (and hence, <i>not</i> defect transitions). Researchers confirmed measurements of improved (5×) hole drift mobilities in some specially prepared a-Si:H samples. Disturbingly, solar cells made with such materials did not show improved efficiencies. Researchers significantly clarified the relationship of ambipolar diffusion-length measurements to hole drift mobilities in a-Si:H, and have shown that the <i>photocapacitance</i> measurements can be interpreted in terms of hole drift mobilities in amorphous silicon. They also completed a survey of thin BP:H and BPC:H films prepared by plasma deposition using phosphine, diborane, trimethylboron, and hydrogen as precursor gases.				
14. SUBJECT TERMS photovoltaics ; high-bandgap materials ; amorphous silicon-based solar cells ; electroabsorption ;				15. NUMBER OF PAGES 53
				16. PRICE CODE
17. SECURITY CLASSIFICATION OF REPORT Unclassified		18. SECURITY CLASSIFICATION OF THIS PAGE Unclassified		19. SECURITY CLASSIFICATION OF ABSTRACT Unclassified
				20. LIMITATION OF ABSTRACT UL